ACS NANO

www.acsnano.org

ARTICLE

Single Condensation Droplet Self-Ejection from Divergent Structures with Uniform Wettability

Nicolò Giuseppe Di Novo,* Alvise Bagolini,* and Nicola Maria Pugno*

Cite This: *ACS Nano* 2024, 18, 8626−8640

Read Online

ACCESS | Metrics & More | Article Recommendations | Supporting Information

ABSTRACT: **Coalescence-induced condensation droplet jumping has been extensively studied for anti-icing, condensation heat transfer, water harvesting, and self-cleaning. Another phenomenon that is gaining attention for potential enhancements is the self-ejection of individual droplets. However, the mechanism underlying this process remains elusive due to cases in which the abrupt detachment of an interface establishes an initial Laplace pressure difference. In this study, we investigate the self-ejection of individual droplets from uniformly hydrophobic microstructures with divergent geometries. We design, fabricate, and test arrays of truncated, nanostructured, and hydrophobic microcones arranged in a square pattern. High-speed microscopy reveals the dynamics of a single condensation droplet between four cones: after cycles of growth and stopped self-propulsion, the suspended droplet self-ejects without abrupt detachments. Through analytical modeling of the droplet in a conical pore as an approximation, we describe the slow isopressure growth phases and the rapid transients driven by surface energy release once a dynamic configuration is reached. Microcones with uniform wettability, in addition to being easier to fabricate, have the potential to enable the self-ejection of all nucleated droplets with a designed size, promising significant improvements in the aforementioned applications and others.**

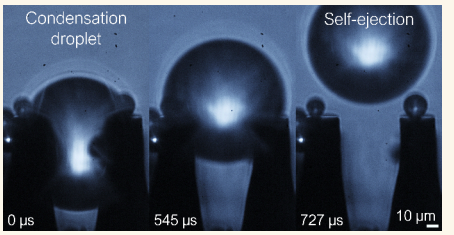

KEYWORDS: *single droplet self-ejection, self-propulsion, condensation, microdroplets, nanostructured microcones, superhydrophobic*

INTRODUCTION

Coalescence-induced condensation droplet jumping (CICDJ) is a fascinating phenomenon observable on natural and artificial surfaces with a certain hydrophobicity and has been highly studied experimentally[1−4] and theoretically[5−9] in the past decade. On a sufficiently hydrophobic surface under condensation conditions, water droplets nucleate, grow, coalesce, and eventually jump, leaving free space where the cycle restarts.[10] During coalescence the excess surface energy is transformed into kinetic energy of translation and oscillation,[9] net of adhesive and viscous losses.[5] The detachment occurs on hydrophobic micro- and/or nanostructured surfaces for their minimal adhesion but with less than 6% efficiency.[11] While for some surfaces of plants[12,13] and insects[14] CICDJ contributes to self-cleaning from pathogens and inert particles, in the academic and industrial fields it is studied for several applications. For example, hydrophilic surfaces structured with microgrooves exploit the flow of small droplets into larger ones through water-filled grooves to improve the drainage of dew collected from the atmosphere.[15,16] Superhydrophobic surfaces provide an alternative as they drain dew through CICDJ and simultaneously possess self-cleaning properties.[17] CICDJ also enhances heat transfer by condensation thanks to the continuous droplet shedding and renucleation of small droplets.[18,19] For these reasons, in frosting conditions, it also provides a passive antifrost effect.[20,21] At negative temperatures, frost is often preceded by condensation.[22] Once a few supercooled droplets freeze spontaneously by homogeneous or heterogeneous nucleation,[23−28] frost percolates governed by the ice-bridging mechanism: the nearby liquid droplets evaporate and desublimate on the frozen ones, forming an ice bridge growing toward them.[20,22,26,29−31] The diameters and distances of the drops determine the success of the ice bridging.[22,31−33] CICDJ slows down frost propagation because it inhibits successful ice bridging.[21,34,35] In recent years, the range of droplet sizes and environmental conditions showing CICDJ has been expanded by other manufacturing ideas and techniques.[1,36,37] To avoid the surface flooding with consequent loss of superhydrophobicity[38] and jumping ability,[39] micro- and nanostructured surfaces capable of spontaneously directing single droplets toward the

Received: July 1, 2023
Revised: February 9, 2024
Accepted: February 13, 2024
Published: February 28, 2024

Downloaded via UNIV DEGLI STUDI DI TRENTO on November 6, 2024 at 11:14:38 (UTC).
See https://pubs.acs.org/sharingguidelines for options on how to legitimately share published articles.

© 2024 American Chemical Society

https://doi.org/10.1021/acsnano.3c05981
ACS Nano 2024, 18, 8626−8640

top of the structures and promote coalescence jumping have been studied.[19,37,40,41]

A topic of growing interest is the single dew microdroplet motion, which broadens the knowledge in wettability and could potentially improve the aforementioned applications among others. Individual droplets, growing within hierarchically nanostructured hydrophobic microstructures, exhibit complete self-ejection at a critical volume. The trigger can be an abrupt change of the microdroplet shape given by either the detachment from the base of the microstructures (experiments with hydrophobic micromesh[42] and rectangular grooves[43]) or the detachment from a strong pinning site (experiments with biphilic V-grooves[43] and simulations with micropyramids[44]). Similarly, single microdroplets growing either between hydrophobic vertical pillars,[41] wedges,[3,45] and irregular cavities[40] or on conical threads[46] self-propel and stop at a certain distance. For both self-ejection and stopped self-propulsion, one interpretation[40,41,43,45] identifies the initiation of motion as the retentive forces are overcome by the pressure force due to the Laplace pressure difference established, before movement, inside the drop.

On the other hand, before any motion, a microdroplet must respect the mechanical equilibrium and thus, by neglecting hydrostatic pressure, must have a uniform internal pressure. Baratian et al.[47] modeled the external forces exerted on a constant-volume static drop positioned within a superhydrophobic wedge. By assuming null contact angle hysteresis, they demonstrated that the resultant is null when the internal pressure is uniform. In particular, for the "menisci" part of the "droplet" system, only the retentive forces enter in the external force system, not the internal Laplace pressure forces. On fixing the volume, the wedge angle, and the equilibrium contact angle, there is a unique equilibrium configuration. Other studies simulated a droplet within an hydrophilic wedge with hysteresis[48] or in a slightly hydrophobic one without hysteresis,[49,50] initially positioned in a out-of-equilibrium configuration: it spontaneously moves and stops at the equilibrium position. The last hydrophobic case represents a particular initial condition of motion whose experimental analogue is the droplet in a superhydrophobic conical capillary, blown by a syringe.[43] At the moment of detachment from the syringe tip, the droplet undergoes an abrupt transition from a mechanical equilibrium to an a out-of-equilibrium configuration, initiating self-propulsion.

The aforementioned individual dew microdroplets[40−43,45] share a common trigger of an out-of-equilibrium state but vary in their growth processes. However, even during quasi-static growth through condensation, mechanical equilibrium must be maintained at all times, as long as there is no net movement of the droplet. It can be presumed that the additional volume is accommodated in a manner ensuring uniform internal pressure, albeit time-varying. Therefore, a Laplace pressure difference does not arise before motion; it is only induced when a critical condition is met, leading to an abrupt change in shape. Notably, an internal Laplace pressure difference emerges during motion, and it is structure- and motion-related.

This alternative description was proposed by Aili et al.[42] for droplets growing between superhydrophobic micromesh structures, initially adhered to the bottom of the structures. The droplet gradually swells at the top of the structures, assuming a stretched shape. Simultaneously, maintaining a uniform internal pressure, it withdraws from the base of the meshes until detachment. The self-ejection of the droplet occurs due to the repositioning of the bottom meniscus on the sidewalls of the mesh, creating a Laplace pressure difference, and also because the surface energy stored in the stretched shape can be released. They did not consider contact angle hysteresis and estimated the velocity of droplet self-ejection through energetic arguments, assuming an efficiency similar to CICDJ.

In this study, we experimentally investigate self-motions that cannot be attributed to an initial Laplace pressure difference induced by abrupt detachment and reconfiguration of a meniscus. We fabricated four surfaces, each consisting of arrays of silicon truncated microcones arranged in a square pattern. These surfaces had the same tapering but different sizes and were uniformly covered by highly hydrophobic nanostructures. Under condensation conditions, we captured individual dew droplets suspended between four microcones using a high-frame-rate camera coupled with a microscope. The dew droplet exhibited an alternating pattern of slow growth and rapid, stopped self-propulsion toward the aperture. Upon reaching the top of the structures, the droplet assumed another dynamic configuration and self-ejected. The self-ejected droplets from the four arrays had a radius range of 9−53 μm, with corresponding self-ejection velocities and transient times of 0.25−0.65 m/s and 46−620 μs, respectively. Utilizing an objective resolution of 500 nm and a minimum frame time of 12.5 μs allowed us to observe that no abrupt detachments occurred. The drop smoothly accelerated once a critical shape was achieved.

To elucidate the physical mechanisms governing growth by condensation, we develop an analytical model based on the assumption of growth with uniform internal pressure, extending it to incorporate contact angle hysteresis.

We give an estimate of the self-ejection velocity on the base of energetic arguments and experimental data. Concurrently, a force-based model is formulated to characterize the transients associated with stopped self-propulsion and self-ejection. Rather than considering the droplet between four cones, for analytical treatment, we examine the droplet within a pore with the same conicity (β), advancing (ϑ_a), and receding (ϑ_r) contact angles. This approximation captures the key elements and also gives good predictions. The differences are discussed. The key aspect of self-motions appears to be the surface energy release triggered when the drop reaches a dynamic configuration, while any abrupt detachment represents an eventual additional effect.

RESULTS

Surface Fabrication and Characterization. To study the growth, self-propulsion, and self-ejection in divergent structures with uniform wettability, we fabricated four arrays of microstructures: truncated microcones arranged in a square pattern by photolithography on silicon (hard mask composed by circles of diameter D_{mask} and pitch p, Table 1) and room-temperature tapered reactive ion etching (t-RIE) (see Figure 1a−c, Materials and Methods, and the Supporting Information for fabrication

Table 1. Design (D_{mask}, p) Parameters and Final Geometry (β, d_h, and l) of the Fabricated and Tested Surfaces

surface	D_{mask} (μm)	pitch p (μm)	tapering β (deg)	head diameter d_h (μm)	height (μm)
10 × 13	10	13	5.8 ± 0.7	5	23.3
15 × 20	15	20	5.7 ± 1	7	34.9
30 × 40	30	40	5.8 ± 0.6	12.5	64.3
60 × 80	60	80	5.5 ± 0.2	31.5	103.7

https://doi.org/10.1021/acsnano.3c05981
ACS Nano 2024, 18, 8626−8640

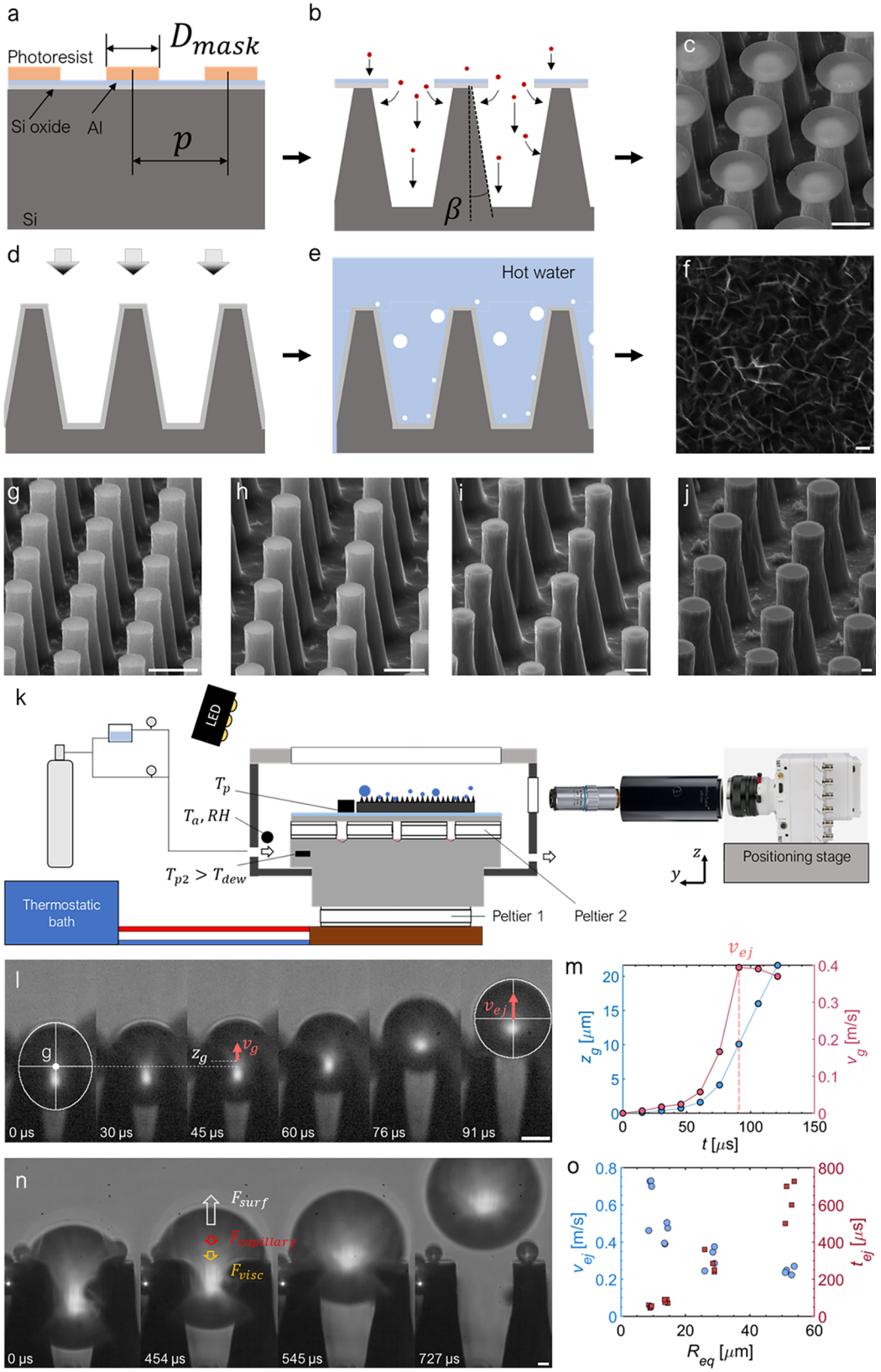

Figure 1. Fabrication steps and experiments. (a) Photolithography, (b) tapered reactive ion etching (t-RIE), (c) scanning electron microscope (SEM) image of Surface 15 × 20 after t-RIE, (d) e-beam evaporation of Al, (e) hot water treatment (HWT), and (f) SEM image of NanoAl. SEM images of truncated microcones all tilted 60° respect to a plane ⊥ to the electron beam: (g) Surface 10 × 13, (h) 15 × 20, (i) 30 × 40, and (j) 60 × 80. (k) Scheme of the experimental setup. (l) Image analysis of a droplet self-ejecting from the nanostructured microcones of Surface 15 × 20 captured at 66000 fps and (m) the relative evolution of position and velocity of the center of mass (g) assumed to be the center of a fitted ellipse. (n) Self-ejection event on the Surface 60 × 80 captured at 11000 fps (see Supplementary video 6). (o) Scatter plot of the experimental self-ejection velocity (v_{ej}) and transient times (t_{ej}) measured for the four surfaces. Scale bars are 10 μm apart from the one of (f) that is 100 nm.

https://doi.org/10.1021/acsnano.3c05981
ACS Nano 2024, 18, 8626−8640

details). We identify the surfaces as "Surface $D_{mask} \times p$". The combined effect of anisotropic and isotropic etching results in pillars with a tapering (β), head diameter (d_h), height (l), and smoothness depending on the t-RIE process parameters, the area fraction free from the hard mask (φ), and the etching time (t_e). With the aim of fabricating four surfaces with the same β, φ, and aspect ratio l/D_{mask} but different sizes, we explored the effects of φ and t_e on β and the etch rate by processing various Si wafers with a lithography mask consisting of 1 cm^2 light-exposed areas patterned with combinations of D_{mask} and p. By analyzing the parameter nonobvious trends we selected four structures (Table 1 and Figure 1g–j) realizable with a similar geometry ($\beta \approx 5.7°$) and the highest possible surface smoothness (see Materials and Methods). We fabricated them on larger areas (2 cm × 10 cm) and cleaved into 2 cm × 2 cm samples. We obtained microcones uniformly covered by aluminum hydroxide nano flakes (NanoAl) (Figure 1d–f) by evaporating pure aluminum on the cleaved samples, followed by hot water treatment (HWT). NanoAl was then rendered highly hydrophobic by conformal fluorosilane deposition (see Materials and Methods). We characterized the wettability of NanoAl by replicating the Al evaporation, HWT, and silanization procedures on flat silicon samples. On NanoAl, with the macro-droplet method, $\vartheta_a = 166 \pm 1°$ and $\vartheta_r = 123 \pm 7°$ while the contact angles obtained with the microdroplet method (the ones used in the modeling and peculiar to the walls of the microstructures) are $\vartheta_a = 157 \pm 1°$ and $\vartheta_r = 145 \pm 6°$ (see Materials and Methods). The dynamic contact angles on hydrophilic and hydrophobic[51] surfaces depend also on the capillary number $Ca = \mu v_{cl}/\sigma_{lv}$, where μ is the dynamic viscosity, v_{cl} the contact line velocity, and σ_{lv} the liquid–vapor surface tension. ϑ_a and ϑ_r measured with the two methods are quasi-static because they pertain to contact lines moving at a very small velocity, thus with a capillary number $Ca \approx 0$. Consequently, using ϑ_a and ϑ_r is reliable for modeling the slow growth but may be an approximation for self-motions. On the other hand, for superhydrophobic rough surfaces, it has been shown that there is no dependence of ϑ_a up to at least $Ca = 0.2$, while ϑ_r decreases marginally with $Ca = -0.2$.[52] The highest velocity at the end of self-ejection of the droplets here studied is 0.7 m/s, resulting in $Ca \approx 0.16$ at 1°C. Therefore, we expect that employing ϑ_a and ϑ_r for motion modeling does not introduce a significant error. We placed the surfaces on a cold plate inside a chamber with controlled humidity and observed the dynamics of condensation droplets with a high-frame-rate camera coupled with a microscope (see Figure 1k and Materials and Methods).

Single Droplet Growth between Truncated Microcones, Self-Propulsion, and Self-Ejection. The condensation droplets nucleate on random sites that can be either the lateral and bottom walls or truncated cone heads. We did not notice preferential sites among the three cases for first-generation nuclei. Apart from the last case, the droplet grows, touches the inner walls of the four cones, and settles symmetrically. The droplet moves toward the aperture by alternating slow growth phases (via condensation) with fast *stopped self-propulsions*, when a dynamic configuration is reached (Supplementary Videos 1 and 2 captured from the side view; see Figure S1). After a time dependent on the unit cell size (in our cases on the order of minutes), the droplets arrives to the top edges, slowly grows to another dynamic configuration (Supplementary Video 2) and rapidly *self-ejects* (Figure 1l,n, Supplementary Videos 3–6 from a side view, Supplementary Video 7 from a top view, and Supplementary Videos 8 and 9 from a side view not perpendicular to the cleavage line). Depending on its volume (radius of the equivalent spherical droplet in the range 9–53 μm), the droplet accelerates to ~0.25–0.65 m/s (*self-ejection velocity*) in ~40–700 μs, respectively, and detaches from the structures (Figure 1l–o). Four events are reported for each surface. Figure 1i shows how we acquired the evolution of the center of mass position and velocity during self-ejection transients (see Materials and Methods).

DISCUSSION

By analyzing the Supplementary Videos, the drop is stretched during the static phases before self-propulsion and self-ejection and resembles a spheroid that intersects the four truncated microcones of a unit cell. The contact areas are pseudoelliptical nonflat surfaces, a complex case to deal with analytically. However, one can observe that the droplet forms two menisci, one facing toward the opening and one toward the base of the microstructures, in contact with the walls of the solid cones. The curvature of each meniscus depends on β and its position and contact angle on the cone. Even a droplet inside a conical pore has two menisci, the curvatures of which depend on the same variables. We here adopt the pore approximation to capture the basic mechanisms. As we will see, it is faithful even quantitatively.

In External Forces and Equilibrium Configurations, the system of external forces acting on the *droplet in a pore* system is described.

In Prepropulsion Growth Phases, by assuming a conical pore with contact angle hysteresis, we identify the geometric configurations of the drop such that it is in mechanical equilibrium. We describe which of these configurations it assumes as it grows by condensation, depending on the initial configuration and contact angles and on tapering. The drop is enabled to move once it reaches a dynamic configuration, in which, thanks to hysteresis, it is stretched.

In Self-Ejection from Microcones: Energetic Modeling, we analyze the experimental dynamic configuration of the droplet between four cones preceding self-ejection and find it to be in good agreement with predictions obtained using the pore model. By treating the droplet between the four cones as a spheroid and employing energetic arguments, we give an estimate of the final self-ejection velocity.

In Self-Propulsion Transient in a Conical Pore: Force Modeling and Self-Ejection Transient from a Conical Pore: Force Modeling, we employ a force-based model to analytically describe the transients of self-propulsion and self-ejection, continuing the analysis with the conical pore. Once the droplet achieves a dynamic configuration, the surface energy of the drop decreases as it moves toward the opening. Consequently, a driving force originates from the surface energy release and leads to acceleration. The motion is opposed by capillary and viscous forces. The pore model retains the essential elements needed to elucidate the observed mechanisms of a drop between solid cones, although differences are discussed.

External Forces and Equilibrium Configurations. We first analyze the forces involved with the aim of describing the quasi-static growth and simulating the rapid motions of a droplet considered as a particle. Let us consider the droplet suspended in a conical pore during growth (Figure 2a) and verify that the Laplace pressure and contact line forces acting on the *top meniscus* system (Figure 2b) are equal and opposite. The droplet is micrometric (radius <100 μm), and gravitational effects can be

https://doi.org/10.1021/acsnano.3c05981
ACS Nano 2024, 18, 8626–8640

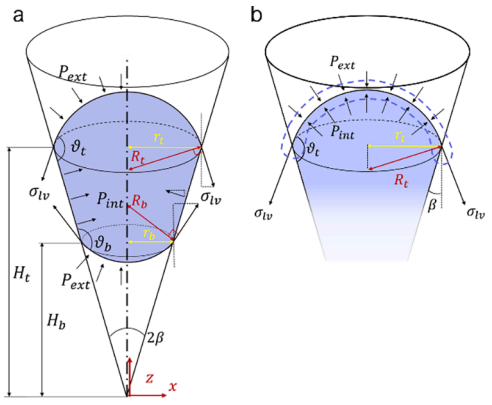

Figure 2. (a) Scheme of a droplet suspended in a hydrophobic conical pore showing half of the forces acting on the droplet system in the *xz* plane: surface tension on the contact lines and pressures on the contact area and caps. (b) Forces acting on the meniscus system, highlighted with the blue dotted line.

safely neglected. For the Laplace pressure $\Delta P_t \equiv P_{int} - P_{ext} = -[2\sigma_{lv}\cos(\vartheta_t + \beta)]/r_t$, the upward (positive z) force $F_{Laplace}$ is $\Delta P_t \cdot A$, where P_{int} and P_{ext} are the internal and external pressures, $A = \pi r_t^2$ is the spherical cap area projected on a plane $\perp$ to z, r_t is the contact radius, σ_{lv} is the liquid−vapor surface tension, β is the half aperture, and ϑ_t is the apparent contact angle on the wall. All the following expressions are written relative to positive z. Thus, $F_{Laplace,t} = -2\pi\sigma_{lv}r_t\cos(\vartheta_t + \beta)$, a force exerted by the droplet bulk on the *meniscus* system. The force exerted by the solid to the *droplet* system, as a reaction of the solid to the surface tension acting on the circular contact line,[53] projected along positive z, is $F_{\sigma,t} = -2\pi\sigma_{lv}r_t\cos(\pi - \vartheta_t - \beta)$, which is equal in modulus to $F_{Laplace,t}$ but opposite.

This result confirms the force balance of the generic meniscus and is, in fact, true by definition. Hence, differently from other studies utilizing the conical pore to approximate a wedge,[43,45] we only insert $F_{\sigma,t}$ into the system of external forces acting on the "*droplet*" system and not $F_{Laplace,t}$ because they would cancel out. The proof for the *bottom* meniscus is analogous.

Regarding the droplet suspended in the conical pore with hysteresis, the contact angles ϑ_t and ϑ_b can vary in the range $[\vartheta_r, \vartheta_a]$. By imposing the curvature radii R_t (eq S1.1) and R_b (eq S1.2) to be equal, we obtain eq 1, the relationship to be satisfied by the five parameters H_t, H_b, ϑ_t, ϑ_b, and β in order to have a uniform internal pressure (as for wedges[48,54−56]). In eq 1 we define the *shape ratio* $\lambda \equiv H_t/H_b$ between the heights of the contact lines respect to the apex. The external forces acting on the *droplet* system are the reaction of the solid to the surface tension acting on the contact lines of both menisci, $F_{\sigma,t}$ and $F_{\sigma,b}$, the reaction of the solid to the internal pressure force acting on the contact area, $F_p = \int[P_{ext} + \Delta P_{Laplace}(z)]\sin\beta\, dA_{truncated\ cone}$, and the atmospheric pressure forces on caps, $F_{cap,t} = -P_{ext}\pi r_t^2$ and $F_{cap,b} = P_{ext}\pi r_b^2$, all projected along the positive verse of the z symmetry axis. Note that the constant atmospheric pressure P_{ext} acting on both caps and contact area (a closed surface) generates a null net force based on Gauss's theorem. Thus, we put $P_{ext} = 0$ to avoid these terms. For a highly hydrophobic conical pore, $F_{\sigma,b}$ and F_p are positive while $F_{\sigma,t}$ is negative. The resultant *capillary* force, $F_{capillary} \equiv F_{\sigma,t} + F_{\sigma,b} + F_p$, depends ultimately on H_t, H_b, ϑ_t, ϑ_b, and β and can be greater or less than 0.

Elsewhere, it has been shown with simulations that an isopressure droplet, in a wedge with hysteresis, has $F_{capillary} = 0$.[48,56] For the present case, the analytical proof is straightforward: $F_{capillary}$ with the three respective terms in explicit form (eq 2) is identically null for every H_t, H_b, ϑ_t, ϑ_b and β that satisfy eq 1 (see section S1, Supporting Information). The third term, F_p, is obtained by substituting $\Delta P_{Laplace} = 2\sigma_{lv}/R_t$.

$$\lambda \equiv \frac{H_t}{H_b} = \frac{\cos(\vartheta_t + \beta)}{\cos(\vartheta_b - \beta)} \tag{1}$$

$$F_{capillary} = -2\pi\sigma_{lv}H_t\tan\beta\cos(\pi - \vartheta_t - \beta) + 2\pi\sigma_{lv}H_b \tan\beta\cos(\pi - \vartheta_b + \beta) + \frac{\pi(r_t + r_b)(H_t - H_b)}{\cos\beta} \cdot\frac{2\sigma_{lv}}{R_t}\sin\beta \tag{2}$$

In other words, given a droplet of a certain volume in the pore, the isopressure configurations are also equilibrium configurations for the external force system. During the slow growth by condensation, a quasi-static process, it is reasonable to assume that the incoming volume redistributes in the possible equilibrium configurations, expressed by eq 1, by adjusting the contact line heights and contact angles of the two menisci.

Prepropulsion Growth Phases. When the droplet nucleates on a lateral wall or on the ground of a surface structured with truncated microcones, it grows, contacts the other cones of a unit cell, swells, and increases the contact area until it positions itself symmetrically between the 4 cones as shown in Video S7. In this context, we are primarily interested in describing analytically the growth process from the symmetric settling onward. Regarding the isopressure configurations, eq 1 and the growth phases described below for the conical pore are a reasonable approximation of the scenario of the droplet between the four cones. This is because the internal pressure is governed by the average curvature of the menisci, which, even in the case of the four cones, relies on the positions and contact angles of both the *top* and *bottom* menisci and on β.

After the settling, we can say that $\lambda \in [\lambda_{min,growth}, \lambda_{max}]$ where $\lambda_{max} = \cos(\vartheta_a + \beta)/\cos(\vartheta_r - \beta)$ and $\lambda_{min,growth} = \cos(\vartheta_r + \beta)/\cos(\vartheta_a - \beta)$ are the limit shape ratios, marked with a red and a black dot, respectively (Figure 3a). In Figure 3a, we represent with black curves the relation between ϑ_b and ϑ_t (from eq 1) for the various λ values allowed. As the volume increases, ϑ_b, ϑ_t, H_b, and H_t evolve following precise paths. We identified two subsequent growth phases: phase 1 which consists of two subcases, both of which end with $\vartheta_t = \vartheta_a$, and phase 2 that ends with $\vartheta_t = \vartheta_a$ and $\vartheta_b = \vartheta_r$, the dynamic configuration with the shape ratio λ_{max}. Figure 3b,c depicts the two phases for both subcases. We describe the detailed evolution of ϑ_b, ϑ_t, H_b, and H_t of the two phases in Section 2.1 in the Supporting Information.

Phase 2 ends with the attainment of λ_{max}, regardless of the initial λ. The *growth phases* can be clearly observed in Supplementary Videos 1 and 2. The shape ratio λ_{max} corresponds to the *dynamic configuration* of self-propulsion with both menisci enabled to move. Considering the average $\beta = 5.7°$, the theoretical $\lambda_{max} = 1.26$ slightly overestimates by 5% the experimental one ($\lambda_{max,exp} = 1.19 \pm 0.02$), calculated by analyzing the droplet shape an instant before self-propulsion (section S2.2 in the Supporting Information). λ_{max} will be employed in Self-Propulsion Transient in a Conical Pore: Force Modeling to simulate stopped self-propulsion of a droplet inside the conical pore.

Self-Ejection from Microcones: Energetic Modeling. *Pre-ejection Growth.* Figure 4a illustrates the directions from

https://doi.org/10.1021/acsnano.3c05981
ACS Nano 2024, 18, 8626−8640

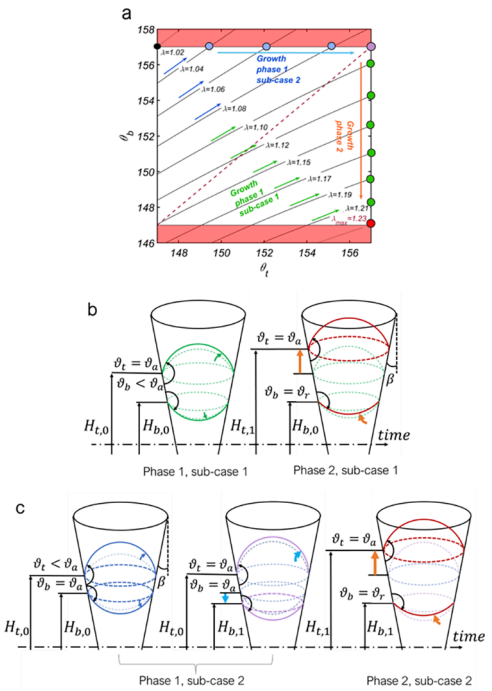

Figure 3. (a) Diagram of the growth phases 1 (with the two subcases) and 2 in terms of ϑ_b and ϑ_t (from eq 1) for various initial shape ratios $\lambda \in [\lambda_{min,growth}, \lambda_{max}]$ where these two extremal values are depicted as a black and a red dot, respectively, for $\beta = 6°$. We set $[\vartheta_r, \vartheta_a] = [147°, 157°]$ as the contact angle range. Any point on a black line represents a possible initial configuration (shadowed regions are not allowed). As the volume increases during phase 1, the system can reach a blue, violet, or green dot following its black line. Then, during phase 2, λ increases to λ_{max}, the dynamic configuration (red dot), regardless of the initial configuration, and the droplet self-propels. The red dotted line represents $\vartheta_b = \vartheta_t$. In (b) and (c) the corresponding illustrations where the caps depicted with dotted lines indicate configurations before the ones with solid lines and colors are referred to the ones of arrows and dots in (a).

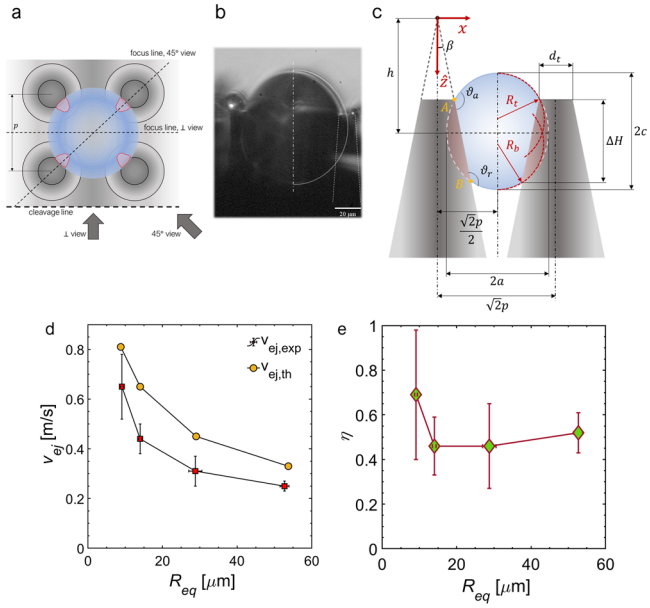

Figure 4. (a) Diagram of the surface with the 3 views used in the experiments: from above (view of (a) itself), perpendicular to the silicon cleavage line, and at 45° to that line. The planes of focus pass through the center of the droplet. (b) Frame of Supplementary Video 8, 45° view, highlighting the elliptical section of the drop. (c) Dimensioned diagram of the drop from the 45° view used for the spheroid model developed in Self-Propulsion Transient in a Conical Pore: Force Modeling. (d) Comparison of $v_{ej,exp}$ and $v_{ej,th}$ (eq 4) for various self-ejection radii (R_{eq}). (e) Self-ejection efficiency (eq 5) as R_{eq} varies.

which Supplementary Videos 1–6 (view perpendicular to the cleavage line of the samples), Supplementary Video 7 (view from above) and Supplementary Videos 8 and 9 (view at 45° to the cleavage line) were recorded. Supplementary Videos 1 and 2 show the droplet pre-ejection growth once it reaches the top edges of the truncated cones after cycles of growth and stopped self-propulsion. *Top* contact radius is fixed, ϑ_t increases, and thus the pressure increases. In parallel, the *bottom* meniscus slightly advances toward the base of the structure (as is clear in Supplementary Video 2), similarly to prepropulsion growth (phase 1, subcase 2) to equal the pressure. If the structure was a conical pore, as we will see in Self-Ejection Transient from a Conical Pore: Force Modeling, then ϑ_t should surpass $\pi - \beta$ to overcome the maximum pressure condition (or alternatively, the condition of minimum curvature radius). It corresponds to $\vartheta_t^* = 90°$, with ϑ_t^* being the top contact angle relative to the head plane. Afterward, ϑ_t would increase, the pressure would decrease, and the *bottom* meniscus would reduce ϑ_b toward ϑ_r (dynamic configuration). However, in the actual case of four cones, ϑ_t reaches ϑ_a, which corresponds to $\vartheta_t^* = 74°$, and stops. Then, the *top* contact line expands laterally slightly, incorporating the cones (Supplementary Videos 8 and 9 and Figure 4b). This detail hints that in complex geometries, the drop assumes shapes that minimize interfacial energy rather than strictly adhering to contact angles locally. The slight lateral expansion implies a decrease in internal pressure driving ϑ_b toward ϑ_r, thus to a dynamic configuration. Subsequently, the droplet accelerates, and ϑ_t increases with a fixed contact radius.

Self-Ejection Velocity. To estimate the self-ejection velocity of a droplet from four cones, we examine its geometry to estimate the surface energy difference between the confined and ejected states. Videos captured from various angles depict the droplet taking on the shape of a spheroid intersecting the four cones. We can conceptualize it as a spheroid generated by the rotation of an ellipse of semiaxes "a" and "c", and with its center at coordinate $(x, \hat{z}) = (\sqrt{2}p/2, h)$, as illustrated in Figure 4b,c. We assume the *top* meniscus to be pinned on the top edge of the cones. By writing the curvature radii of the top and bottom menisci considering them in the advancing and receding conditions, respectively, and by imposing their equality (isopressure condition), we estimate "a", "c", and the spheroid surface area $A_{spheroid}$ and its volume $V_{spheroid}$ (Section S3 in the Supporting Information), an instant before the transient.

The radius of a sphere of the same volume is $R_{eq,th} = [3V_{spheroid}/(4\pi)]^{1/3}$. If the difference in surface energy between the initial and final states (eq 3) were fully converted into kinetic energy, the droplet would have the self-ejection velocity expressed in eq 4. For now, we neglect adhesion energy since the cone walls are highly hydrophobic—an estimate of the equilibrium contact angle is $\vartheta_{eq} = \cos^{-1}[(\cos\vartheta_a + \cos\vartheta_r)/2] \approx 150°$—and because the contact areas are a minor part of the lateral interface (Figure 4a and Supplementary Video 7). By dividing the experimental kinetic energy $\rho V_{exp} v_{ej,exp}^2/2$, where $v_{ej,exp}$ and V_{exp} are the experimental ejection velocity and volume, respectively, by the theoretical one (assuming a total conversion

https://doi.org/10.1021/acsnano.3c05981
ACS Nano 2024, 18, 8626–8640

Table 2. Experimental Data and Modeling Results for the Droplets on the Four Surfaces

surface	a_{exp} (μm)	a (μm)	c_{exp} (μm)	c (μm)	$R_{eq,exp}$ (μm)	$R_{eq,th}$ (μm)	$v_{ej,exp}$ (m/s)	$v_{ej,th}$ (m/s)	η
10 × 13	8	8.04	10.6 ± 0.3	10.57	9.1 ± 0.4	8.81	0.65 ± 0.13	0.81	0.69 ± 0.29
15 × 20	13	12.78	15.9 ± 0.1	16.83	14.0 ± 0.5	14.01	0.44 ± 0.06	0.65	0.46 ± 0.13
30 × 40	27.5	26.47	33.0 ± 0.6	34.85	28.8 ± 1.7	29.01	0.31 ± 0.06	0.45	0.46 ± 0.19
60 × 80	48.5	49.03	59.3 ± 0.9	64.57	52.7 ± 1.2	53.74	0.25 ± 0.02	0.33	0.52 ± 0.09

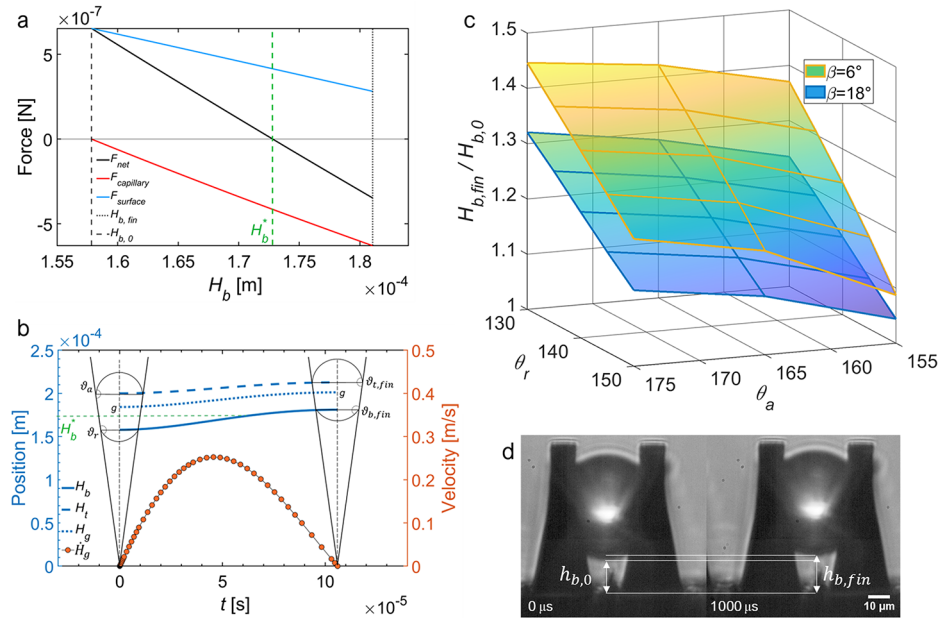

Figure 5. (a) F_{net}, $F_{capillary}$, F_{surf} as a function of H_b for a droplet with equivalent radius R_{eq} = 24.7 μm, ϑ_a = 157°, ϑ_r = 145°, and β = 6. H_b* (green dotted line) corresponds to F_{net} = 0. $H_{b,0}$ is the initial condition while its final value, $H_{b,fin}$, results from solving eq 9 and stopping the calculations at $\dot{H}_b$ = 0. (b) Time evolution of the droplet considering viscous dissipations: position of H_b, H_g, and H_t with respect to the cone apex and the velocity of the center of mass, $\dot{H}_g$. (c) 3D map of $H_{b,fin}/H_{b,0}$ vs ϑ_a, ϑ_r, and β for the nonviscous case. (d) Example of droplet self-propulsion recorded at 1000 fps by testing a Surface 30 × 40 and illustration of the measurement of h_b.

of surface to kinetic energy), we express the efficiency of self-ejection from the four cones (η) as in eq 5. We report the experimental data and model results for the four surfaces (Table 2), compare $v_{ej,exp}$ with $v_{ej,th}$ (Figure 4d), and plot η (Figure 4e) for the various self-ejection radii. The model well-estimates "a" and "c". Indeed, the average relative error of $R_{eq,th}$ compared to $R_{eq,exp}$ is 0.1%. The imposition of the isopressure condition for the droplet between cones implicitly assumes the shape ratio λ_{max} found with the pore model (Section S3 in the Supporting Information). Consequently, the accurate estimation of the spheroid further affirms the appropriateness of the conical pore approximation. Figure 4d shows that the model follows the experimental trend well and, as we expect, overestimates the final ejection velocity. In fact, the total conversion of $\Delta E_{surf,cones}$ into kinetic energy neglects the viscous, adhesion and contact line dissipations. $\eta \approx 50\%$ reveals that self-ejection is much more efficient than coalescence-induced jumping ($\eta < 6\%$).

$$\Delta E_{surf,cones} = \sigma_{lv}(A_{spheroid} - 4\pi R_{eq,th}^{\ 2}) \tag{3}$$

$$v_{ej,th} = \sqrt{\frac{2\Delta E_{surf,cones}}{\rho V_{spheroid}}} \tag{4}$$

$$\eta = \frac{\rho V_{exp} v_{ej,exp}^{\ 2}}{2\Delta E_{surf,cones}} \tag{5}$$

Self-Propulsion Transient in a Conical Pore: Force Modeling. In this section, we analytically examine the transient of stopped self-propulsion using a force-based model. Given the requirement for precise knowledge of the droplet's geometry and contact area to describe the forces, we utilize the approximation of a droplet in a conical pore. This approximation, despite differences to describe (at the end of Self-Ejection Transient from a Conical Pore: Force Modeling), retains the essential elements that govern the motion of a droplet between four solid cones. The theoretical framework for simulating the droplet motion is then taken up in the self-ejection section where we directly compare the modeled and experimental motions.

During the growth by condensation in a confined space, the droplet surface energy, $E_{surf,pore}$, is stored in a geometrical configuration dependent on the contact angle hysteresis and compatible with the isopressure condition. Once λ_{max} is attained, the motion toward the aperture is enabled and the system evolves toward configurations with lower $E_{surf,pore}$. We consider the volume to be constant during the transients as the motion occurs in tens to hundreds of μs and the condensation volume is negligible. Also, we assume the liquid to be incompressible. In reference to Figure 2a, we derived the expression for the volumes and forces (see also eqs S4.1−S4.7). The general expression of the droplet volume in such a pore is V (eq S4.1), the sum of the top and bottom spherical caps, and of the truncated cone volumes, respectively (eqs S4.2−S4.4). The self-propulsion volume V* of a particular simulated droplet can be calculated

https://doi.org/10.1021/acsnano.3c05981
ACS Nano 2024, 18, 8626−8640

with eq S4.1 by choosing $\vartheta_b = \vartheta_r$, $\vartheta_t = \vartheta_a$, an initial H_b, called $H_{b,0}$, and an initial H_t, called $H_{t,0}$, which is $\lambda_{max}H_{b,0}$. During sliding toward the aperture, H_b and H_t vary but the caps contact angles and the volume V^* keep constant. Thus, by imposing $V^* = V$, we find H_t expressed as a function of H_b which stands during all the motion (eq S4.7). For each simulated droplet, any geometrical quantity and force can be expressed as a function of the lone H_b and its time derivatives. $E_{surf,pore}$ is expressed in eq 6 (explicit form in eq S4.5). Under these hypotheses, $E_{surf,pore}$ is the potential of a driving surface force F_{surf} (eq 7),[57−60] positive as H_b increases for the case considered here.

$$E_{surf,pore} = \sigma_{lv}(A_{cap,t} + A_{cap,b} - A_{truncated\ cone}\cos\vartheta_{eq}) \quad (6)$$

$$F_{surf} = -\frac{dE_{surf,pore}}{dH_b} \quad (7)$$

At the same time, the external force system, $F_{capillary}(H_b)$, acts on the droplet. $F_{\sigma,b}$ is the same as that of eq 2 (second term) while for $F_{\sigma,t}$ (first term) we substitute H_t with eq S4.7. As the droplet moves away from the isopressure configuration, the two curvatures evolve differently and thus there is an internal pressure gradient. We modify F_p to eq S4.6 by assuming a linear pressure profile $P(z) = p_b + (\Delta p_t - \Delta p_b)(z - H_b)/(H_t - H_b)$, in similarity to what is employed elsewhere for wedges.[50] The infinitesimal area of the truncated cone is $dA = 2\pi \tan(\beta)\, z\, dz/\cos\beta$ with $z \in [H_b, H_t]$. $\Delta p_t = 2\sigma_{lv}/R_t$, $\Delta p_b = 2\sigma_{lv}/R_b$, and $p_b = \Delta p_b + P_{ext}$ are the top and bottom Laplace pressure differences and the bottom pressure, respectively. Again, the force contribution of P_{ext} on the truncated cone area balances with those on the two caps, so, for calculation purposes, we place it equal to zero and do not consider F_{caps}. With substitutions and by solving the integral in z, also F_p is a function of H_b alone (see eq S4.6).

$F_{capillary}$ is negative as the droplet moves toward the aperture (an opposing force). The net force $F_{net} = F_{capillary} + F_{surf}$ is positive until $H_b = H_b^*$ (Figure 5a): the droplet accelerates, decelerates, and stops. The motion is driven by a position-dependent force $F_{net}(H_b)$ acting on the droplet center of mass H_g, a function of the lone $H_b(t)$ (see Section S4.2 in the Supporting Information). In addition, the walls oppose a viscous force $F_{visc} = \tau \cdot A$ to the droplet as it slides, with τ and A being the shear stress and contact area, respectively. By assuming a Poiseuille flow in a tube of radius r and for small β, the fluid velocity profile can be approximated as $v(x) = \dot{H}_g[1 - (x/r)^2]$, $\tau = \mu(dv/dx)|_{x=r}$, $A \approx 2\pi r(H_t - H_b)$, and the viscous force[61] as in eq 8 with $\dot{H}_g$ being the velocity of the center of mass and μ the dynamic viscosity. Considering the drop as a particle accelerating under the effect of the resultant force $F_{tot} \equiv F_{net} - F_{visc} = F_{surf} + F_{capillary} - F_{visc}$, we obtain eq 9, where ρ is the water density and $\ddot{H}_g$ the acceleration of the droplet center of mass.

$$F_{visc} = 4\pi\mu\dot{H}_g(H_t - H_b) \quad (8)$$

$$\ddot{H}_g\rho V^* = F_{tot} \quad (9)$$

By substituting the expressions of $\dot{H}_g$ and $\ddot{H}_g$ as functions of H_b, $\dot{H}_b$, and $\ddot{H}_b$ into eq 9 and solving numerically in MATLAB, we obtained $H_b(t)$ and $\dot{H}_b(t)$ (details in Section S4.3 in the Supporting Information). The developed code detects particular events such as reaching a prescribed $H_b^{\#}$ or when $\dot{H}_b = 0$ and stops the calculations. Then, by substituting the H_b and $\dot{H}_b$ numerical values in H_g and $\dot{H}_g$, we plotted the motion of the center of mass (example in Figure 5b). In Section S4.4, we provide a qualitative interpretation of the self-propulsion and self-ejection trigger.

The droplet does not stop at $F_{net} = 0$ (identified by H_b^* in Figure 5a,b) but at a certain final $H_{b,fin}$. For self-propulsion, the solver is interrupted when the drop stops ($\dot{H}_b = 0$) because before any eventual acceleration in the opposite direction, under the effect of the negative $F_{capillary}$, the contact angles should be reconfigured (*bottom* in advancing and *top* in receding conditions) and $F_{capillary}$ rewritten accordingly. Indeed, during the propulsion and in the stop position, $F_{capillary} < 0$ (Figure 5a) because $F_{\sigma,t}$ is negative and greater in modulus than the positive $F_{\sigma,b} + F_p$ and thus the internal pressure is not uniform. In particular, the meniscus top has a larger pressure. Right after the stop and before the eventual motion toward the negative direction, the contact lines are fixed and the contact angles rearrange to cancel the internal pressure difference. If $\lambda_{fin} = H_{t,fin}/H_{b,fin}$ and the particular volume V^* do not allow an isopressure configuration but one with higher pressure at the top meniscus, the droplet reaches the dynamic configuration for traveling in the negative z, accelerates, stops, and so on. For the parameters ϑ_a, ϑ_r, and β of interest in this study we found that the droplets can re-equilibrate in the stop position (identified by $H_{b,fin}$) and calculated which final $\vartheta_{t,fin}$ and $\vartheta_{b,fin}$ are attained by the menisci starting from ϑ_a and ϑ_r, respectively (Section S4.4 in the Supporting Information). Figure S2 shows $H_{b,fin}/H_{b,0}$, $\vartheta_{t,fin}$, and $\vartheta_{b,fin}$ for various equivalent radii R_{eq} (the radius of a spherical droplet with the same volume V^*), for both the viscous and nonviscous cases and fixed surface parameters. It is interesting to note that all three quantities are independent of droplet size for the nonviscous case while varying marginally in the viscous one. With multiple simulations we built a 3D map of $H_{b,fin}/H_{b,0}$ for various ϑ_a, ϑ_r, and β, considering the nonviscous case (Figure 5c): as a guideline, we deduce that $H_{b,fin}/H_{b,0}$ increases with ϑ_a and with the contact angle hysteresis while it decreases with β. In addition to those shown in Supplementary Videos 1 and 2, we captured and analyzed other four self-propulsion events. All the videos were captured from the view $\perp$ to the cleavage line (see Figure 5d and Figure S1) from which the actual point of contact of the meniscus bottom with the walls cannot be seen; the ideal view would be at 45°, but it does not allow good illumination of the meniscus bottom as the light is blocked by the cones behind it; we therefore measured $h_{b,0}$ and $h_{b,fin}$ (Figure 5d) and calculated the experimental $H_{b,fin}/H_{b,0} = 1.05 \pm 0.02$ (analogously to Section S2 in the Supporting Information). The viscous model predicts $H_{b,fin}/H_{b,0} \approx 1.14$ for the droplet captured, thus overestimating the experimental value by ∼8%. The transient time of self-propulsion was not the main scope of the present article; however, we captured at 2000 fps the self-propulsion of a droplet with R_{eq} similar to the simulated one (Figure 5a) and it takes place between two frames, thus in less than 500 μs. We here have predicted that self-propulsion causes a small displacement, a fraction of the droplet size, as observed in the present experiments and in others with droplets in wedges.[3,45]

Self-Ejection Transient from a Conical Pore: Force Modeling. As demonstrated in Results, the droplet alternates between growth phases and self-propulsions until the *top* meniscus reaches the heads of the truncated cones. Then, it grows and self-ejects as described in Self-Ejection from Microcones: Energetic Modeling. In the conical pore analogy the droplet reaches $H_{t,max}$ with a self-ejection shape ratio (λ_{ej}). We will illustrate that λ_{ej} is not unique but history-dependent. Let us analyze the growth and subsequent self-ejection in the

https://doi.org/10.1021/acsnano.3c05981
ACS Nano 2024, 18, 8626−8640

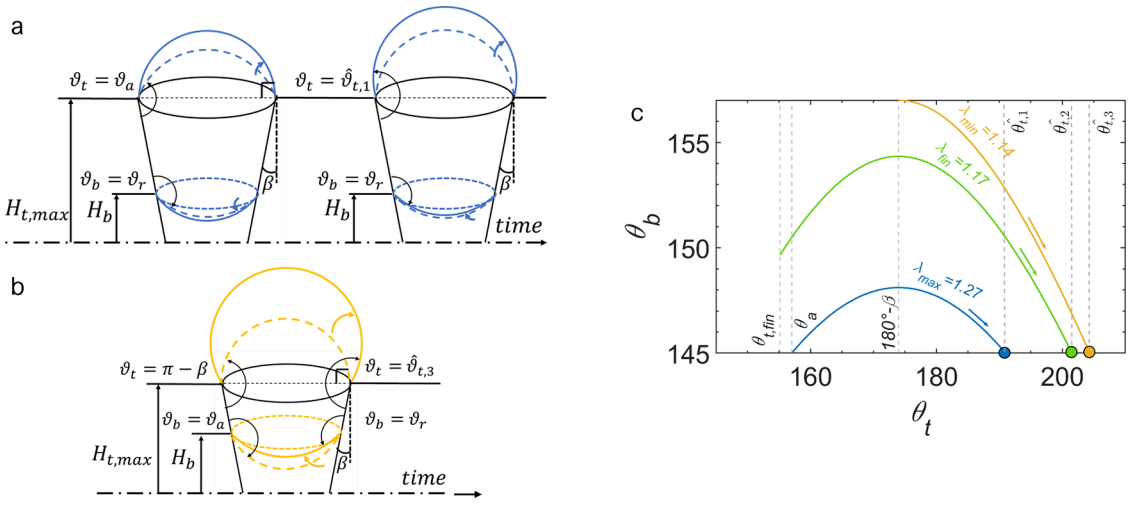

Figure 6. Schemes of the pre-self-ejection growth in Case 1 (a) and Case 3 (b). The caps depicted with dotted lines indicate configurations earlier than those with solid lines and colors are referred to (c) where the contact angle evolution (from eq 1) of the three cases is plotted for the parameters β = 6°, ϑ_a = 157°, and ϑ_a = 145°. Cases 1−3 are depicted in blue, green and yellow, respectively.

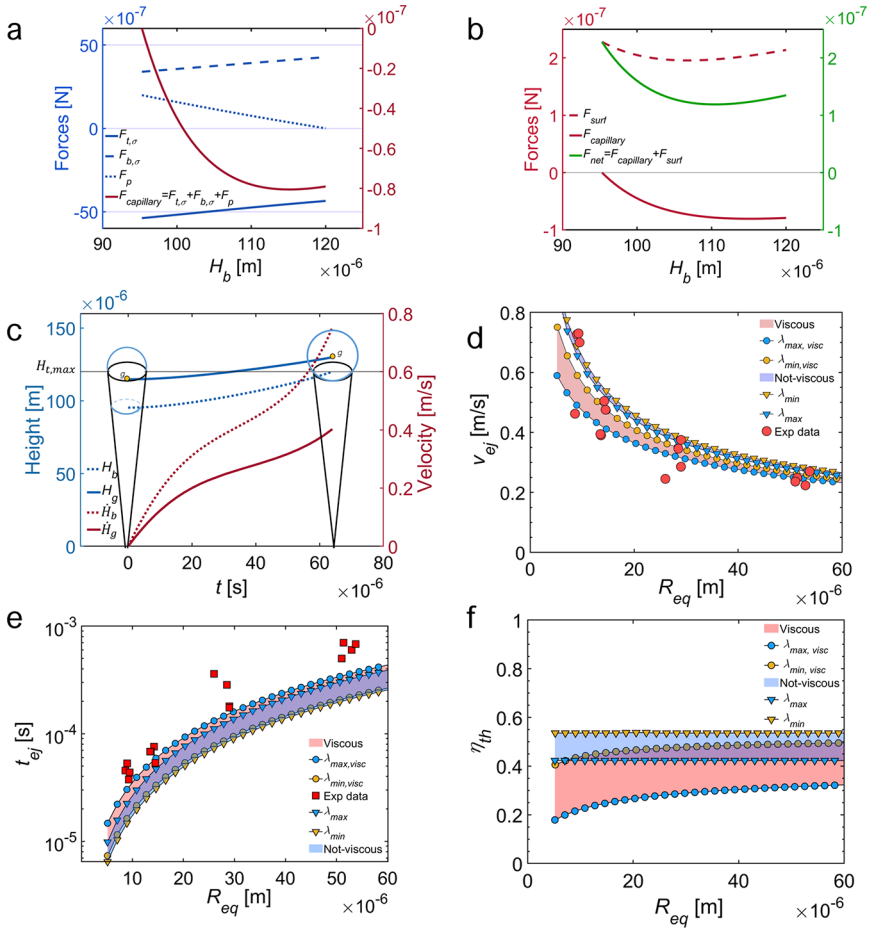

Figure 7. Evolution of forces (a, b) $H_b(t)$ and $H_g(t)$ and (c) their velocities for a droplet with R_{eq} = 14.7 μm and λ_{max}. (d) Comparison of the experimental data with the theoretical ranges of the final self-ejection velocity of the center of mass and (e) transient time for different equivalent radii for both the viscous and nonviscous cases and fixed surface parameters β = 5.7°, ϑ_a = 157°, and ϑ_a = 145°. (f) Theoretical efficiency n_{th} (eq 10) as the equivalent radii varies for both the viscous and nonviscous cases.

framework of the conical pore approximation. For the conical pore model we assume the respect of local contact angles: thus, the pre-ejection growth by condensation does not imply the lateral enlargement of the *top* meniscus (fixed at $H_{t,max}$) but the increase of ϑ_t (toward ϑ_a measured with respect to the heads of the truncated cones, a plane $\perp$ to z). As the volume increases, the contact angles of the two menisci evolve to overcome the striction imposed by the edge until *bottom* reaches ϑ_r (the *self-*

https://doi.org/10.1021/acsnano.3c05981
ACS Nano 2024, 18, 8626−8640

ejection dynamic configuration) and the droplet self-ejects by releasing $E_{surf,pore}$. We shall elaborate upon the differences with the actual scenario at the end of this section.

Pre-Self-Ejection Growth. We consider the growth as a quasi-static process with uniform pressure at each instant as in Prepropulsion Growth Phases. λ_{ej} can be between two extreme values to be identified among three possible cases. ***Case 1***: the drop is exactly at the end of growth phase 2 which would result in self-propulsion if the droplet is not at the edge; therefore, when $H_t = H_{t,max}$, $\lambda_{ej,1}$ coincides with λ_{max}, which is the maximum shape ratio allowed (Figure 6a). ***Case 2***: the droplet has just finished a self-propulsion and stops exactly with $H_{t,fin} = H_{t,max}$; thus, $\lambda_{ej,2}=\lambda_{fin}$, $\vartheta_b = \vartheta_{b,fin}$ and $\vartheta_t = \vartheta_{t,fin}$. ***Case 3***: the droplet nucleated near the edge (H_t is already equal to $H_{t,max}$) and only goes through *growth phase 1* (subcase 2) described for prepropulsion growth (Figure 6b). The shape ratio $\lambda_{ej,3}$, coincident with λ_{min} (defined in Section S5), is the smallest possible. Details of the shape ratios and contact angles evolution of each case can be found in Section S5 in the Supporting Information. We plot the contact angle evolution in Figure 6c by using eq 1 and by considering the three λ_{ej} described.

The pre-self-ejection growth analysis and Figure 6c reveal that, for any parameters β, ϑ_a, ϑ_r of the surface and $H_{t,max}$, the ejection shape ratio (λ_{ej}), the ejection volume (V_{ej}), and the *top* contact angle at the beginning of motion ($\hat{\vartheta}_t$) are history dependent. In particular, they depend on the initial bottom meniscus height, $H_{b,0}$, which determines the number of self-propulsions (zero, one, two or more) the droplet will make to reach the edge. Since $H_{b,0}$ is a random variable depending on the nucleation site, we will study the two extreme cases (1 and 3) being $\lambda_{min} \le \lambda_{ej} \le \lambda_{max}$.

Self-Ejection Transient. Once a droplet has reached one of the possible dynamic configurations (a certain λ_{ej} to which certain $\hat{\vartheta}_t$ and V_{ej} values correspond) and accelerates under the effect of F_{tot}, the displacement at constant volume occurs with an increase of H_b at constant $\vartheta_b = \vartheta_r$ and with an increase of ϑ_t at constant $H_t = H_{t,max}$. By setting $V_{ej} = V$, with V of the general equation S4.1, V_{ej} a particular value, and ϑ_b and H_t being constants, ϑ_t depends on the lone H_b during the motion (see Section S5 in the Supporting Information). All the forces are also functions of $H_b(t)$ alone.

For the experimental β, ϑ_a, and ϑ_r, we solved eq 9 numerically for the two extreme shape ratios λ_{min} and λ_{max} and for various $H_{t,max}$ to simulate different droplet volumes. The calculations were stopped when the condition $H_b = H_{t,max}$ is verified, which corresponds to the instant in which the droplet has a null contact area and detaches. $\dot{H}_g$ in that instant is the theoretical self-ejection velocity, $v_{ej,th}$. Figure 7a,b shows the evolution of the force terms and Figure 7c depicts H_b, H_g, and their velocities for a droplet with λ_{max}. Figure 7d,e compares the experimental self-ejection velocity ($v_{ej,exp}$) of the center of mass and transient times with the theoretical ranges ($v_{ej,th}$ and t_{ej} for λ_{min} and λ_{max}) for various equivalent radii, for both the viscous and not viscous cases. In Figure 7f, the theoretical efficiency η_{th} is

$$\eta_{th} = \frac{\rho V_{ej} v_{ej,th}^{\ 2}}{2\Delta E_{surf,pore}} \tag{10}$$

where the theoretical kinetic energy is divided by $\Delta E_{surf,pore} = E_{surf,initial} - E_{surf,final}$. $\Delta E_{surf,pore}$, the surface energy difference between the initial and final state of self-ejection from a conical pore, represents the maximum kinetic energy that the droplet would gain if there were no viscous, adhesion and contact line dissipations. The model predicts $v_{ej,exp}$ very well both qualitatively and quantitatively. The energy dissipated by capillary forces (~45−60%) exceeds that dissipated by viscous ones (~15−25%). The experimental $\eta \approx 50\%$ falls in the range of η_{th} in the viscous case (20−55%). Interestingly it is much higher than that of coalescence-induced jumping (<6%).

Figure 8 presents a comparison between the experimental and simulated transients of droplets with the same volume. The

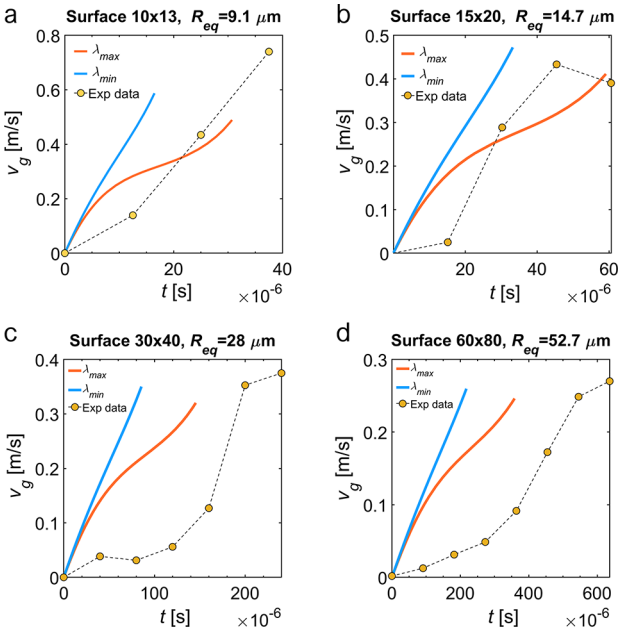

Figure 8. Comparison between experimental (Supplementary Videos 3−6) and modeled (viscous case) self-ejection transients of (a) Surface 10 × 13, captured at 80000 fps, (b) Surface 15 × 20, captured at 66000 fps, (c) Surface 30 × 40, captured at 25000 fps, and (d) Surface 60 × 80, captured at 11000 fps. We set the simulated volume equal to the experimental one.

model tends to underestimate the transient time as the droplet size increases (Figure 7e and 8). This delay may be attributed to the way in which the edge striction is overcome in the actual scenario of four solid cones, as described in Self-Ejection from Microcones: Energetic Modeling: not during the pre-ejection growth as in the model but rather during the self-ejection process itself. As the droplet accelerates, the opposing $F_{t,\sigma}$ is a decreasing function in the modeled case, while it exhibits a maximum when $\vartheta_t = \pi - \beta$ in the real case (vertical surface tension forces), thereby delaying the velocity ramp. However, once the striction is overcome in the real case, velocity slopes similar to the simulated ones indicate well-estimated accelerations $F_{tot}/(\rho V^*)$ and thus force F_{tot}, being equal the experimental and simulated volumes.

It is important to clarify that the current pore model effectively captures the underlying physics of the real case transients by considering all the relevant forces (F_{surf}, $F_{capillary}$, and F_{visc}), helps in understanding the mechanism, and can be employed to well predict the self-ejection velocity trends and magnitude. However, it remains an approximation, as it assumes a contact area in the shape of a frustum of a cone instead of four nonplanar pseudoellipse-shaped contact areas. The actual case would have the capillary forces expressed in another fashion, the contact area and surface tension vectors being different. Also viscous and surface forces would be different due to a reduced contact area.

https://doi.org/10.1021/acsnano.3c05981
ACS Nano 2024, 18, 8626−8640

In addition, the internal flow is not simulated and we expect more complex velocity and pressure fields, implying different internal dissipations. Three-dimensional fluid dynamics simulations may clarify these points and provide a more accurate estimate of the process.

CONCLUSIONS

In this study, we captured the evolution of individual microdroplets of condensation between truncated, nanostructured, and hydrophobic microcones with high temporal and spatial resolutions. This allowed us to visualize in detail the various growth phases and self-motions of the droplet confined in a diverging structure with contact angle hysteresis. It emerges that both stopped self-propulsion and self-ejection, while rapid, do not occur through abrupt detachment and reconfiguration of a meniscus. The droplet accelerates gradually as soon as it reaches a critical configuration dependent on advancing and receding angles and geometry. The self-ejection radius is precisely controlled by the structures' geometry differently from coalescence jumping, where it is a random variable. The self-ejection velocity decreases with droplet radius.

Through the approximation of the conical pore, we theoretically analyzed the forces at play in various phases and simulated the self-motions. It is deduced that as long as the droplet grows by condensation, it must pass through configurations with uniform internal pressure. Once the critical configuration is reached, motion begins for the release of surface energy. Our models predict well both the self-ejection velocity magnitude and trend with the radius as well as the transient dynamics and the self-ejection efficiency. The efficiency is estimated to be around 50%, far higher than coalescence-induced condensation droplet jumping (<6%).

In other works reporting self-ejection, the motion is often described as triggered by the Laplace pressure difference. However, in our case, we have observed that initially the pressure must be uniform to grant mechanical equilibrium. Therefore, we attempt to provide clarification regarding these scenarios. In the case of a droplet in a superhydrophobic V-groove[43] or between micropyramids,[44] both with the *bottom* meniscus pinned to a hydrophilic site, we expect the droplet to have on average a uniform internal pressure before detachment from the site as it is static. As soon as it detaches, the *bottom* meniscus reconfigures on the hydrophobic walls and quickly reaches a Laplace pressure greater than the *top*. If this situation is described with the forces expressed in the present paper, it would be $F_{capillary} > 0$ in the first part of acceleration. The droplet accelerates until ejection thanks to both $F_{capillary}$ and F_{surf}.

In the case of a rectangular groove[43] of half-aperture δ, on the other hand, the droplet fills the entire groove before swelling above the edge. In fact, the edge acts as a constriction that requires the *top* meniscus to reach the minimum radius of curvature (δ) to be overcome. With a filled groove, the *bottom* meniscus is in contact with the base of the surface structure. The droplet grows, and once it swells beyond the constriction, the pressure decreases, and consequently, the *bottom* meniscus retracts due to the isopressure condition. When it detaches, it quickly reconfigures on the vertical walls with a pressure greater than the *top* ($F_{capillary} > 0$), and the droplet accelerates. As it advances toward the opening, the pressure difference increases (thus, $F_{capillary}$), and thanks also to F_{surf}, the droplet self-ejects. The explanation for this case is analogous to the self-ejection from the micromesh one.[42]

In our case, however, the droplet accelerates due to F_{surf} alone, and $F_{capillary}$ starts from zero and is negative during motion (opposing force): an instant before ejection, the *top* Laplace pressure is indeed greater than the *bottom* one. In general, it is inferred that the irreducible driving force of droplet self-motions is F_{surf}, which can act as soon as the droplet has reached a dynamic configuration. Particular detachments and geometric conditions may impose pressure differences between the two menisci that either favor or oppose the motion. Note that neglecting F_{surf}, the critical condition for ejection becomes $R_t \geq -r_b/\cos(\theta_b - \beta)$ that for $\beta = 0$ identically recovers the Marmur's prediction.[87] Accordingly, this model could be considered a generalization of the Marmur's approach (which cannot explain the self-ejection of a droplet from a cylindrical capillary), including, conicity, hysteresis, energy release driving force and related transient mechanism.

In future theoretical and experimental studies we aim to investigate self-ejection from microcones as advancing and receding contact angles and cone geometry vary. By preliminary evaluations with our model, we expect lower limit values of the receding angle and upper limit values of the tapering beyond which the self-ejection does not occur. The present research describes and proves experimentally the self-ejection from microcones in its essentiality. We prove self-ejection from divergent structures without the need of pinning sites to induce an abrupt detachment[44] which is beneficial for fabricability and scalability. It will be possible to adapt our model to the case of self-propulsion and/or ejection caused by abrupt detachments.

Moreover, we deduce that microcones with a small head area fraction (with a sharp tip) would reduce the percentage of droplets that nucleate on the heads and can only leave the surface by coalescence jumping. In this way, all the droplets would leave the surface by self-ejecting at a precise, designed size without the variability typical of coalescence jumping. To obtain this result on a surface structured with rectangular microgrooves would mean to reduce the wall thickness toward zero with the consequent instability and poor mechanical resistance. Microcones with a small head area fraction, instead, would maintain mechanical resistance because of a growing cross-section, higher for larger β. Future studies will explore the optimal β that allow self-ejection and provide the highest mechanical resistance.

We would like to mention that other jumping modes have been observed on our surfaces: confined and unconfined droplets can coalesce and jump in various combinations: for example, in Supplementary Video 8. The different scenarios and their effects on the dynamics of the droplet population will be addressed in future studies.

The authors felt that this class of surfaces could bring further enhancements in the applications where coalescence jumping has already introduced improvements.

MATERIALS AND METHODS

Microstructure Fabrication. We employed 6 in. silicon wafers (100) as the substrate to fabricate microcones by photolithography and tapered reactive ion etching (t-RIE) (Figure 1a–c). After a standard RCA cleaning, the hard mask was made by growing 200 nm of thermal silicon oxide (Centrotherm E1200HT furnace) followed by the deposition of 200 nm of aluminum by magnetron sputtering (Eclipse MRC). Then we deposited 1.2 μm of positive photoresist by spin coating (Track SVG). We employed two photolithographic masks (Photronics).

(1) Mask1 consists of areas of 1 cm × 1 cm with arrays of circles arranged either in a square or hexagonal pattern, each with a different circle diameter (D_{mask}) and pitch (p) (green areas in

https://doi.org/10.1021/acsnano.3c05981
ACS Nano 2024, 18, 8626–8640

Table S1). It was designed to investigate the effect of the nonmasked area fraction, of D_{mask}, of the pattern type, and of the etching time on the t-RIE in terms of microstructure tapering, etch rate, and surface characteristics such as the roughness of the walls and the presence of grass on the bottom. The patterns are transferred on the photopolymer-coated wafers by one-step UV-light exposure (mask aligner MA150CC).

(2) After the studies with Mask1 we designed Mask2 with circles arranged in a square pattern with optimal D_{mask} and p (Table 1). The square pattern allows condensation droplets to be observed against high-intensity backlighting, a crucial aspect for acquisitions at high frame rates (see Condensation Experiments). Mask2 is for use with a stepper photolithographic machine (Nikon 2205i11D), and its pattern was reproduced on large areas, as depicted in Figure S7, by stacking various UV-light expositions. Working over large areas facilitates the manipulation required in the subsequent phases and in particular the cleavage with the breaking line passing over the pattern and parallel to the rows of cones.

After the developing (Track SVG), a hard bake of the photopolymer was carried out. The pattern transfer onto the hard mask was performed by dry etching of aluminum (KFT Metal PlasmaPro100 Cobra300) and silicon oxide (Tegal 903e). Then the t-RIE step was performed (Alcatel dry etcher). The scallops typical of the deep reactive ion etching (DRIE)[62,63] may be strong pinning sites for droplets and frustrate the self-ejection. Therefore, we opted for continuous etching[64,65] using SF_6-C_4F_8 plasma,[66] a process without scallops and in which the ratio of gas flows, chamber pressure, bias and source power, and temperature influence the tapering and uniformity of the sidewalls. We developed a t-RIE recipe with the purpose of creating truncated microcones with tapering angle (β, see Figure S3a) in the range 5−10° and as similar as possible among the four arrays different in size to be tested in condensation conditions. Also, the etch rate has to be preferably higher than 500 nm/min and the lateral and bottom walls as smooth as possible. The recipe parameters are source power 2800 W, bias power 20 W, gas flux ratio SF_6/C_4F_8 = 0.65, total gas flux 500 sccm, chamber pressure 0.04 mbar, and wafer temperature 20 °C. The evidence of the campaign of experiments carried out with Mask1 is that β is the result of vertical etching and horizontal etching under the mask and is constant from the bottom base up to about three-fourths of the microstructure, then it goes to zero on top; β and the etch rate have a peaked trend with the etching time, for each particular mask geometry; β has either a decreasing or a peaked trend with the unmasked area fraction φ; for $\varphi >$ 0.7, irregularities of the lateral and bottom walls of the microstructures (ribs) appear; the mean etch rate is 680 ± 80 nm/min. In Section 6.1 in the Supporting Information we report the measurement method of β and images and plots in support of the mentioned trends.

Then we fabricated the four patterns (Mask2) to test in condensation conditions, designed with $D_{mask} \times p$ optimal to minimize wall irregularities and with similar β (Figure 1g−j and Table 1). This β is a medium one relative to the upper part of the microstructures involved in self-ejection (see Section 6.1 in the Supporting Information). It is on average the same for the four surfaces and equal to 5.7°. We removed the etching passivation layer by immersion in isopropanol with ultrasonic pulses and then the hard mask by dipping the wafers in an Al etch solution and then in a silicon oxide etch solution. We cleaned them in a deionized water rinse until the bath reached 16 MΩ cm. The truncated microcones have, some more than others, an undercut at the apex. We removed it with isotropic etching (Tegal 900) which lowered the pillars by about 2 μm and made straight the top part (see Section 6.1 in the Supporting Information).

Nanostructuring, Silanization, and Wettability. As a second hierarchical level we have selected the aluminum to be nanostructured (NanoAl) with hot water treatment (HWT) as compatible with clean room processes; the structuring is simple, cheap, and scalable and could also be used for microstructures produced directly on aluminum through other industrial processes. The hot water treatment of many metals and their alloys leads to the formation of nanostructures. A thin superficial layer of metal oxide forms in hot water and the oxide cations are released in solution, migrate, and deposit, forming nanostructures with peculiar shapes for each metal.[67,68] In the case of Al, thin nanoblades of hydrated aluminum oxide (pseudoboehmite) are formed which, once made hydrophobic, have shown superhydrophobic and antifreezing properties.[69−75] Both water temperature and treatment time have an effect on contact angles.[72,76,77] We deposited 150 nm of pure Al on the wafers by e-beam evaporation (ULVAC HIGH VACUUM COATER EBX-16C) (Figure 1.d). The wafers were cleaved as shown in Figure S7 in order to have samples with a row of cones on the sharp edge. HWT was performed by immersion in deionized water (18 MΩ cm) at 90 °C for 7 min (Figure 1e), immediately followed by immersion in room temperature deionized water to block the structuring and then dried with a N_2 flow. The SEM image of the nanostructures in Figure 1f was done with a Tescan SEM. We cleaned the surfaces by dipping in acetone, isopropanol, and deionized water, dried with a N_2 flow, and activated the surfaces with oxygen plasma (to increase the amount of silanols and maximize the uniformity and density of the self-assembled monolayer[78]). Chemical vapor deposition (CVD)[79−82] of 1*H*,1*H*,2*H*,2*H*-perfluorodecyltriethoxysilane (Sigma-Aldrich) was performed by placing the samples and 200 μL of fluorosilane in a sealed (class IP-67) aluminum box (internal volume of 3.7 L) heated at 150 °C for 3 h followed by an annealing for 1.5 h with the box opened (for covalently unbound silane removal).

To characterize the advancing and reeding contact angles of water on the walls of the microcones we measured them on the non-microstructured areas of the samples, only covered by NanoAl (Figure S9). We characterized them with two procedures.

(1) Macro-droplets: we employed a syringe pump (Pump 11 Elite, Harvard apparatus) to inject and aspirate a droplet of deionized water at a volume rate of 3 μL/min (to avoid dynamic effects[83]) through a syringe with diameter 230 μm (gauge 32), positioned close to and perpendicular to the surface. We captured the two steps with a digital microscope (Dinolite AM7915MZTL) and measured the contact angles with DropSnake,[84] an ImageJ plug-in. The values were acquired when the droplet has a diameter at least 5 times the syringe diameter: $\vartheta_a = 166 \pm 1°$ and $\vartheta_r = 123 \pm 7°$.

(2) Microdroplets: we captured the micro droplets (tens of μm) during condensation and evaporation with the experimental setup described in the next paragraph (Phantom camera + microscopy objective) and analyzed with DropSnake. $\vartheta_a = 157 \pm 1°$ and $\vartheta_r = 145 \pm 6$. We used the microdroplet contact angles for the analytical models, as they are characteristic of the microdroplets affected by growth, self-propulsion, and self-ejection, accounting only for the capillary and not inertial effects. The macrodroplets are instead influenced by the gravitational force.

The equilibrium contact angle of NanoAl can be estimated using the experimental contact angles[85] with $\vartheta_{eq,NanoAl} = \cos^{-1}[(\cos \vartheta_a + \cos \vartheta_r)/2] \approx 150°$. A theoretical estimate can be obtained by applying the Cassie−Baxter equation,[86] $\cos \vartheta_{CB} = f(\cos \vartheta_{eq,flat} + 1) - 1$. With the microdroplet procedure on a flat Si surface, covered by e-beam evaporated Al and silanized, we measured $\vartheta_{a,flat} = 111.4 \pm 0.2°$ and $\vartheta_{r,flat} = 89.8 \pm 1.5°$; thus, $\vartheta_{eq,flat} = 100°$. With ImageJ's *Particle Analysis* plug-in we roughly quantified the area fraction of the solid−liquid interface ($f \approx 0.17$) (Figure S10), thus $\cos \vartheta_{CB} \approx 149°$. The good agreement with $\vartheta_{eq,NanoAl}$ suggests that droplets are in a fakir state on NanoAl.

Condensation Experiments. We performed the condensation experiments in a custom-made setup (see Figure 1k for the setup scheme) according to the following procedure: we introduced the desired humid air in a chamber (800 cm^3) by mixing a dry and a wet air flux. The wet air flux iswas obtained by passing dry air in a bubbler filled with deionized water (18 MΩ cm). Each flux was set with a flow meter (FR2000, Key instruments), and the total flux was 800 sccm. The relative humidity (RH) and temperature of the mixed air (T_p) were measured with an Arduino BME280 sensor (accuracies ±3% and ±1 °C) placed at the chamber inlet. The cold plate inside the chamber was cooled by a thermostatic bath and two Peltier stages to T_p = 1 °C (measured with a thin film PT100 thermocouple, RS pro, class B

https://doi.org/10.1021/acsnano.3c05981
ACS Nano 2024, 18, 8626−8640

accuracy) for the duration of the experiments. The sample and the PT100 were in thermal contact with the cold plate through a thermal pad (T-flex 600 Series Thermal Gap Filler, Laird Technologies, thickness of 1 mm, thermal conductivity of 3 W/mK). Given the low thermal inertia of the silicon samples (thick 600 μm) and the PT100, we assume surface temperature $T_{surf} = T_p$. The water vapor pressure (P_{vap}) of the fluxed air is 11.8 hPa; thus, the saturation ratio on the sample surface was $s = P_{vap}/P_{vap,sat}(T_{surf}) = 1.8$, where $P_{vap,sat}(T_{surf})$ is the saturation vapor pressure at T_{surf}. We placed the sample on the plate, introduced dry air, and cooled to $T_{surf} = 1$ °C. Then, humid air was introduced and condensation started. The chamber was equipped with an upper and a lateral quartz window. To observe condensation (and evaporation, for the microdroplet contact angle measurements) we employed a high-frame-rate camera (Phantom Veo 640, Vision Research) coupled to a microscopy objective (50× Mitutoyo Plan Apo infinity corrected, long working distance 13 mm, resolving power 500 nm, depth of focus 900 nm) through a tube lens (InfiniTube Ultima, magnification 0.8×). We illuminated the surfaces with an LED light (MULTILED QT, GSVITEC) placed outside the environmental chamber and on the back of the samples with respect to the video camera. The growth and self-propulsion videos were captured at 24−2000 fps while self-ejection transients were captured at 9000−80000 fps. The transient frames were analyzed in ImageJ to measure the position (z_g) evolution of the center of mass (g) considered as the center of a fitted ellipse (Figure 1l). The velocity at the instant i, $v_g(i)$, is calculated as $[z_g(i) - z_g(i-1)]/\Delta t$, with Δt being the time length of a frame. A 3-axis micro positioning stage was used to move the camera and to focus.

ASSOCIATED CONTENT

Supporting Information

The Supporting Information is available free of charge at https://pubs.acs.org/doi/10.1021/acsnano.3c05981.

Video S1: Single droplet growth, self-propulsion, and self-ejection on Surface 15 × 20, ⊥ view (MP4)
Video S2: Single droplet growth, self-propulsion, and self-ejection on Surface 30 × 40, ⊥ view (MP4)
Video S3: Single droplet self-ejection transient on Surface 10 × 13, ⊥ view (AVI)
Video S4: Single droplet self-ejection transient on Surface 15 × 20, ⊥ view (AVI)
Video S5: Single droplet self-ejection transient on Surface 30 × 40, ⊥ view (AVI)
Video S6: Single droplet self-ejection transient on Surface 60 × 80, ⊥ view (AVI)
Video S7: Single droplet self-ejection transient on Surface 60 × 80, top view (AVI)
Video S8: Single droplet self-ejection transient on Surface 30 × 40, 45° view, example 1 (AVI)
Video S9: Single droplet self-ejection transient on Surface 30 × 40, 45° view, example 2 (AVI)
Geometrical analysis and equilibrium of a droplet suspended in a conical pore with uniform internal pressure, growth phases and calculations of the shape ratio λ_{max}, self-ejection from four cones, energetic modeling, expressions and relations between variables in self-propulsion and self-ejection for the conical pore model, self-ejection from a conical pore, fabrication, and details of Supplementary Videos 1−9 (PDF)

AUTHOR INFORMATION

Corresponding Authors

Nicolò Giuseppe Di Novo − *Laboratory of Bioinspired, Bionic, Nano, Meta, Materials & Mechanics, Department of Civil, Environmental and Mechanical Engineering, University of Trento, 38123 Trento, Italy; Center for Sensors and Devices, Fondazione Bruno Kessler, 38123 Trento, Italy;* orcid.org/0000-0002-7540-0434; Email: nicolo.dinovo@unitn.it

Alvise Bagolini − *Center for Sensors and Devices, Fondazione Bruno Kessler, 38123 Trento, Italy*; Email: bagolini@fbk.eu

Nicola Maria Pugno − *Laboratory of Bioinspired, Bionic, Nano, Meta, Materials & Mechanics, Department of Civil, Environmental and Mechanical Engineering, University of Trento, 38123 Trento, Italy; School of Engineering and Materials Science, Queen Mary University of London, London E1 4NS, United Kingdom;* orcid.org/0000-0003-2136-2396; Email: nicola.pugno@unitn.it

Complete contact information is available at: https://pubs.acs.org/10.1021/acsnano.3c05981

Author Contributions

N.G.D.N. and A.B. designed the study and designed and fabricated the surfaces. N.G.D. tested the surfaces, analyzed and interpreted the data, developed the modeling, and wrote the manuscript. A.B. and N.M.P. discussed the modeling and edited the manuscript. A.B. and N.M.P. supervised the research.

Notes

The authors declare no competing financial interest.

ACKNOWLEDGMENTS

We kindly thank Alberto Bellin, Luigi Fraccarollo, and Fabio Sartori (University of Trento, Italy) who lent us the Phantom camera, Elia Scattolo (FBK, Trento, Italy) for the SEM images of the nanostructures, the Micro Nano Facility technical staff (FBK, Trento, Italy) for support in the fabrication. A special thanks to Stefano Siboni and Claudio Della Volpe (University of Trento, Italy) for fruitful discussions on the model. The study has been supported by the European Commission under the FET Open "Boheme" grant no. 863179 and by the UE-FESR-MUR-PO Ricerca e Innovazione progetto STREAM ARS_01_01182.

REFERENCES

(1) Mouterde, T.; Lehoucq, G.; Xavier, S.; Checco, A.; Black, C. T.; Rahman, A.; Midavaine, T.; Clanet, C.; Quéré, D. Antifogging Abilities of Model Nanotextures. *Nat. Mater.* **2017**, *16* (6), 658−663.
(2) Chen, X.; Patel, R. S.; Weibel, J. A.; Garimella, S. V. Coalescence-Induced Jumping of Multiple Condensate Droplets on Hierarchical Superhydrophobic Surfaces. *Sci. Rep.* **2016**, *6*, 1−11.
(3) Han, T.; Kwak, H. J.; Kim, J. H.; Kwon, J. T.; Kim, M. H. Nanograssed Zigzag Structures to Promote Coalescence-Induced Droplet Jumping. *Langmuir* **2019**, *35* (27), 9093−9099.
(4) Mouterde, T.; Nguyen, T. V.; Takahashi, H.; Clanet, C.; Shimoyama, I.; Quéré, D. How Merging Droplets Jump off a Superhydrophobic Surface: Measurements and Model. *Phys. Rev. Fluids* **2017**, *2* (11), 1−7.
(5) Wang, F. C.; Yang, F.; Zhao, Y. P. Size Effect on the Coalescence-Induced Self-Propelled Droplet. *Appl. Phys. Lett.* **2011**, *98* (5), 053112.
(6) Chen, Y.; Lian, Y. Numerical Investigation of Coalescence-Induced Self-Propelled Behavior of Droplets on Non-Wetting Surfaces. *Phys. Fluids* **2018**, *30* (11), 112102.
(7) Wang, Y.; Ming, P. Dynamic and Energy Analysis of Coalescence-Induced Self-Propelled Jumping of Binary Unequal-Sized Droplets. *Phys. Fluids* **2019**, *31* (12), 122108.
(8) Lecointre, P.; Mouterde, T.; Checco, A.; Black, C. T.; Rahman, A.; Clanet, C.; Quéré, D. Ballistics of Self-Jumping Microdroplets. *Phys. Rev. Fluids* **2019**, *4* (1), 24−26.

(9) Wasserfall, J.; Figueiredo, P.; Kneer, R.; Rohlfs, W.; Pischke, P. Coalescence-Induced Droplet Jumping on Superhydrophobic Surfaces: Effects of Droplet Mismatch. *Phys. Rev. Fluids* **2017**, *2* (12), 1−17.
(10) Birbarah, P.; Chavan, S.; Miljkovic, N. Numerical Simulation of Jumping Droplet Condensation. *Langmuir* **2019**, *35* (32), 10309−10321.
(11) Enright, R.; Miljkovic, N.; Sprittles, J.; Nolan, K.; Mitchell, R.; Wang, E. N. How Coalescing Droplets Jump. *ACS Nano* **2014**, *8* (10), 10352−10362.
(12) Lv, C.; Hao, P.; Yao, Z.; Song, Y.; Zhang, X.; He, F. Condensation and Jumping Relay of Droplets on Lotus Leaf. *Appl. Phys. Lett.* **2013**, *103* (2), 021601.
(13) Nath, S.; Ahmadi, S. F.; Gruszewski, H. A.; Budhiraja, S.; Bisbano, C. E.; Jung, S.; Schmale, D. G.; Boreyko, J. B. Sneezing" Plants: Pathogen Transport via Jumping-Droplet Condensation. *J. R. Soc. Interface* **2019**, *16* (155), 20190243.
(14) Wisdom, K. M.; Watson, J. A.; Qu, X.; Liu, F.; Watson, G. S.; Chen, C. H. Self-Cleaning of Superhydrophobic Surfaces by Self-Propelled Jumping Condensate. *Proc. Natl. Acad. Sci. U. S. A.* **2013**, *110* (20), 7992−7997.
(15) Bintein, P. B.; Lhuissier, H.; Mongruel, A.; Royon, L.; Beysens, D. Grooves Accelerate Dew Shedding. *Phys. Rev. Lett.* **2019**, *122* (9), 98005.
(16) Kundanati, L.; Di Novo, N. G.; Greco, G.; Siboni, S.; Della Volpe, C.; Bagolini, A.; Pugno, N. M. Multifunctional Roles of Hairs and Spines in Old Man of the Andes Cactus: Droplet Distant Coalescence and Mechanical Strength. *Phys. Fluids* **2022**, *34* (1), 012003.
(17) Haechler, I.; Park, H.; Schnoering, G.; Gulich, T.; Rohner, M.; Tripathy, A.; Milionis, A.; Schutzius, T. M.; Poulikakos, D. Exploiting Radiative Cooling for Uninterrupted 24-h Water Harvesting from the Atmosphere. *Sci. Adv.* **2021**, *7* (26), 1−10.
(18) Zhang, P.; Maeda, Y.; Lv, F.; Takata, Y.; Orejon, D. Enhanced Coalescence-Induced Droplet-Jumping on Nanostructured Superhydrophobic Surfaces in the Absence of Microstructures. *ACS Appl. Mater. Interfaces* **2017**, *9* (40), 35391−35403.
(19) Han, T.; Choi, Y.; Na, K. M.; Kim, M. H.; Jo, H. J. Enhanced Condensation on a Biphilic-Zigzag Surface Due to Self-Arrangement of Crystals on a Micro-Structured Surface. *Int. J. Heat Mass Transfer* **2021**, *179*, 121710.
(20) Boreyko, J. B.; Collier, C. P. Delayed Frost Growth on Jumping-Drop. *ACS Nano* **2013**, *7* (2), 1618−1627.
(21) Zhao, G.; Zou, G.; Wang, W.; Geng, R.; Yan, X.; He, Z.; Liu, L.; Zhou, X.; Lv, J.; Wang, J. Competing Effects between Condensation and Self-Removal of Water Droplets Determine Antifrosting Performance of Superhydrophobic Surfaces. *ACS Appl. Mater. Interfaces* **2020**, *12* (6), 7805−7814.
(22) Nath, S.; Boreyko, J. B. On Localized Vapor Pressure Gradients Governing Condensation and Frost Phenomena. *Langmuir* **2016**, *32* (33), 8350−8365.
(23) Li, L.; Liu, Z.; Zhao, L.; Li, Y. The Theoretical Analysis and Experimental Study on Anti-Frosting Performance of Surface Characteristics. *Int. J. Therm. Sci.* **2019**, *137*, 343−351.
(24) Varanasi, K. K.; Hsu, M.; Bhate, N.; Yang, W.; Deng, T. Spatial Control in the Heterogeneous Nucleation of Water. *Appl. Phys. Lett.* **2009**, *95* (9), 1−4.
(25) Piucco, R. O.; Hermes, C. J. L.; Melo, C.; Barbosa, J. R. A Study of Frost Nucleation on Flat Surfaces. *Exp. Therm. Fluid Sci.* **2008**, *32* (8), 1710−1715.
(26) Liu, J.; Jiang, Y.; Liu, K.; Wang, J.; Zeng, X. C.; Song, Y.; Zhu, C.; Francisco, J. S. Distinct Ice Patterns on Solid Surfaces with Various Wettabilities. *Proc. Natl. Acad. Sci. U. S. A.* **2017**, *114* (43), 11285−11290.
(27) Schutzius, T. M.; Jung, S.; Maitra, T.; Eberle, P.; Antonini, C.; Stamatopoulos, C.; Poulikakos, D. Physics of Icing and Rational Design of Surfaces with Extraordinary Icephobicity. *Langmuir* **2015**, *31* (17), 4807−4821.
(28) Walker, C.; Lerch, S.; Reininger, M.; Eghlidi, H.; Milionis, A.; Schutzius, T. M.; Poulikakos, D. Desublimation Frosting on Nano-engineered Surfaces. *ACS Nano* **2018**, *12*, 8288−8296.
(29) Petit, J.; Bonaccurso, E. General Frost Growth Mechanism on Solid Substrates with Different Stiffness. *Langmuir* **2014**, *30* (4), 1160−1168.
(30) Guadarrama-Cetina, J.; Mongruel, A.; González-Viñas, W.; Beysens, D. Percolation-Induced Frost Formation. *Epl* **2013**, *101* (1), 16009.
(31) Nath, S.; Ahmadi, S. F.; Boreyko, J. B. How Ice Bridges the Gap. *Soft Matter* **2020**, *16* (5), 1156−1161.
(32) Hauer, L.; Wong, W. S. Y.; Sharifi-Aghili, A.; Kondic, L.; Vollmer, D. Frost Spreading and Pattern Formation on Microstructured Surfaces. *Phys. Rev. E* **2021**, *104* (4), 1−7.
(33) Shen, Y.; Zou, H.; Wang, S. Condensation Frosting on Micropillar Surfaces - Effect of Microscale on Ice Propag. *Langmuir* **2020**, *36*, 13563.
(34) Chu, F.; Lin, Y.; Yan, X.; Wu, X. Quantitative Relations between Droplet Jumping and Anti-Frosting Effect on Superhydrophobic Surfaces. *Energy Build.* **2020**, *225*, 110315.
(35) Chen, X.; Ma, R.; Zhou, H.; Zhou, X.; Che, L.; Yao, S.; Wang, Z. Activating the Microscale Edge Effect in a Hierarchical Surface for Frosting Suppression and Defrosting Promotion. *Sci. Rep.* **2013**, *3*, 1−8.
(36) Mulroe, M. D.; Srijanto, B. R.; Ahmadi, S. F.; Collier, C. P.; Boreyko, J. B. Tuning Superhydrophobic Nanostructures to Enhance Jumping-Droplet Condensation. *ACS Nano* **2017**, *11* (8), 8499−8510.
(37) Sharma, C. S.; Stamatopoulos, C.; Suter, R.; Von Rohr, P. R.; Poulikakos, D. Rationally 3D-Textured Copper Surfaces for Laplace Pressure Imbalance-Induced Enhancement in Dropwise Condensation. *ACS Appl. Mater. Interfaces* **2018**, *10* (34), 29127−29135.
(38) Jo, H.; Hwang, K. W.; Kim, D.; Kiyofumi, M.; Park, H. S.; Kim, M. H.; Ahn, H. S. Loss of Superhydrophobicity of Hydrophobic Micro/Nano Structures during Condensation. *Sci. Rep.* **2015**, *5*, 5−10.
(39) Olceroglu, E.; McCarthy, M. Self-Organization of Microscale Condensate for Delayed Flooding of Nanostructured Superhydrophobic Surfaces. *ACS Appl. Mater. Interfaces* **2016**, *8* (8), 5729−5736.
(40) Sharma, C. S.; Combe, J.; Giger, M.; Emmerich, T.; Poulikakos, D. Growth Rates and Spontaneous Navigation of Condensate Droplets Through Randomly Structured Textures. *ACS Nano* **2017**, *11* (2), 1673−1682.
(41) Lv, C.; Hao, P.; Zhang, X.; He, F. Dewetting Transitions of Dropwise Condensation on Nanotexture-Enhanced Superhydrophobic Surfaces. *ACS Nano* **2015**, *9* (12), 12311−12319.
(42) Aili, A.; Li, H.; Alhosani, M. H.; Zhang, T. Unidirectional Fast Growth and Forced Jumping of Stretched Droplets on Nanostructured Microporous Surfaces. *ACS Appl. Mater. Interfaces* **2016**, *8* (33), 21776−21786.
(43) Feng, J.; Miljkovic, N.; Yan, X.; Qin, Y.; Chen, F.; Zhao, G.; Sett, S.; Hoque, M. J.; Rabbi, K. F.; Zhang, X.; Wang, Z.; Li, L.; Chen, F. Laplace Pressure Driven Single-Droplet Jumping on Structured Surfaces. *ACS Nano* **2020**, *14* (10), 12796−12809.
(44) Stendardo, L.; Milionis, A.; Kokkoris, G.; Stamatopoulos, C.; Sharma, C. S.; Kumar, R.; Donati, M.; Poulikakos, D. Out-of-Plane Biphilic Surface Structuring for Enhanced Capillary-Driven Dropwise Condensation. *Langmuir* **2023**, *39* (4), 1585−1592.
(45) Yan, X.; Chen, F.; Sett, S.; Chavan, S.; Li, H.; Feng, L.; Li, L.; Zhao, F.; Zhao, C.; Huang, Z.; Miljkovic, N. Hierarchical Condensation. *ACS Nano* **2019**, *13* (7), 8169−8184.
(46) Wang, Q.; Yao, X.; Liu, H.; Quéré, D.; Jiang, L. Self-Removal of Condensed Water on the Legs of Water Striders. *Proc. Natl. Acad. Sci. U. S. A.* **2015**, *112* (30), 9247−9252.
(47) Baratian, D.; Cavalli, A.; Van Den Ende, D.; Mugele, F. On the Shape of a Droplet in a Wedge: New Insight from Electrowetting. *Soft Matter* **2015**, *11* (39), 7717−7721.
(48) Ataei, M.; Chen, H.; Tang, T.; Amirfazli, A. Stability of a Liquid Bridge between Nonparallel Hydrophilic Surfaces. *J. Colloid Interface Sci.* **2017**, *492*, 207−217.
(49) Ruiz-Gutiérrez, É.; Semprebon, C.; McHale, G.; Ledesma-Aguilar, R. Statics and Dynamics of Liquid Barrels in Wedge Geometries. *J. Fluid Mech.* **2018**, *842*, 26−57.

https://doi.org/10.1021/acsnano.3c05981
ACS Nano 2024, 18, 8626−8640

(50) Ruiz-Gutierrez, E.; Ledesma-Aguilar, R. Lattice-Boltzmann simulations of the dynamics of liquid barrels. *J. Phys.: Condens. Matter* **2020**, *32*, 214007.
(51) Mohammad Karim, A.; Rothstein, J. P.; Kavehpour, H. P. Experimental Study of Dynamic Contact Angles on Rough Hydrophobic Surfaces. *J. Colloid Interface Sci.* **2018**, *513*, 658−665.
(52) Kim, J. H.; Kavehpour, P.; Rothstein, J. P. Dynamic Contact Angle Measurements on Superhydrophobic Surfaces. *Phys. Fluids* **2015**, *27* (3), 032107.
(53) Durand, M. Mechanical Approach to Surface Tension and Capillary Phenomena. *Am. J. Phys.* **2021**, *89* (3), 261−266.
(54) Han, T.; Noh, H.; Park, H. S.; Kim, M. H. Effects of Wettability on Droplet Movement in a V-Shaped Groove. *Sci. Rep.* **2018**, *8* (1), 2−11.
(55) Xu, W.; Lan, Z.; Peng, B.; Wen, R.; Chen, Y.; Ma, X. Directional Movement of Droplets in Grooves: Suspended or Immersed? *Sci. Rep.* **2016**, *6*, 1−11.
(56) He, X.; Cheng, J. Evaporation-Triggered Directional Transport of Asymmetrically Confined Droplets. *J. Colloid Interface Sci.* **2021**, *604*, 550−561.
(57) Liu, T.; Li, Y.; Li, X.; Sun, W. Mechanism Study on Transition of Cassie Droplets to Wenzel State after Meniscus Touching Substrate of Pillars. *J. Phys. Chem. C* **2017**, *121* (18), 9802−9814.
(58) Li, H.; Aili, A.; Alhosani, M. H.; Ge, Q.; Zhang, T. Directional Passive Transport of Microdroplets in Oil-Infused Diverging Channels for Effective Condensate Removal. *ACS Appl. Mater. Interfaces* **2018**, *10* (24), 20910−20919.
(59) Liu, J.; Feng, Z.; Ouyang, W.; Shui, L.; Liu, Z. Spontaneous Movement of a Droplet on a Conical Substrate: Theoretical Analysis of the Driving Force. *ACS Omega* **2022**, *7* (24), 20975−20982.
(60) McCarthy, J.; Vella, D.; Castrejón-Pita, A. A. Dynamics of Droplets on Cones: Self-Propulsion Due to Curvature Gradients. *Soft Matter* **2019**, *15* (48), 9997−10004.
(61) De Gennes, P.-G.; Brochard-Wyart, F.; Quéré, D. Dynamics of Impregantion. *Capillarity and Wetting Phenomena. Drops, Bubbles, Pearls, Waves*; Springer: 2004; Vol. *1*, pp 129−130.
(62) Roxhed, N.; Griss, P.; Stemme, G. Tapered Deep Reactive Ion Etching: Method and Characterization. *TRANSDUCERS 2007 - 2007 International Solid-State Sensors, Actuators and Microsystems Conference, Lyon, France*, 2007; pp 493−496, DOI: 10.1109/SENSOR.2007.4300175.
(63) Lin, P.; Xie, X.; Wang, Y.; Lian, B.; Zhang, G. A Multi-Step Etch Method for Fabricating Slightly Tapered through-Silicon Vias Based on Modified Bosch Process. *Microsyst. Technol.* **2019**, *25* (7), 2693−2698.
(64) Li, R.; Lamy, Y.; Besling, W. F. A.; Roozeboom, F.; Sarro, P. M. Continuous Deep Reactive Ion Etching of Tapered via Holes for Three-Dimensional Integration. *J. Micromechanics Microengineering* **2008**, *18* (12), 125023.
(65) Figueroa, R. F.; Spiesshoefer, S.; Burkett, S. L.; Schaper, L. Control of sidewall slope in silicon vias using plasma etching in a conventional reactive ion etching tool. *J. Vac. Sci. Technol. B* **2005**, *23* (5), 2226−2231 1 September.
(66) Saffih, F.; Con, C.; Alshammari, A.; Yavuz, M.; Cui, B. Fabrication of Silicon Nanostructures with Large Taper Angle by Reactive Ion Etching. *J. Vac. Sci. Technol. B, Nanotechnol. Microelectron. Mater. Process. Meas. Phenom.* **2014**, *32* (6), 06FI04.
(67) Saadi, N. S.; Hassan, L. B.; Karabacak, T. Metal Oxide Nanostructures by a Simple Hot Water Treatment. *Sci. Rep.* **2017**, *7* (July), 1−8.
(68) Vedder, W.; Vermilyea, D. A. Aluminum + Water Reaction. *Trans. Faraday Soc.* **1969**, *65*, 561−584.
(69) Balordi, M.; Santucci de Magistris, G.; Chemelli, C. A Novel Simple Anti-Ice Aluminum Coating: Synthesis and In-Lab Comparison with a Superhydrophobic Hierarchical Surface. *Coatings* **2020**, *10*, 111.
(70) Kim, A.; Lee, C.; Kim, H.; Kim, J. Simple Approach to Superhydrophobic Nanostructured Al for Practical Antifrosting Application Based on Enhanced Self-Propelled Jumping Droplets. *ACS Appl. Mater. Interfaces* **2015**, *7* (13), 7206−7213.
(71) Tudu, B. K.; Kumar, A.; Bhushan, B. Facile approach to develop anti-corrosive superhydrophobic aluminium with high mechanical, chemical and thermal durability. *Philos.Trans.R.Soc.A* **2019**, *377*, 20180272.
(72) Balordi, M.; Cammi, A.; Chemelli, C.; Magistris, G. S. De.; Chimica, D. Role of Nano-Structured Boehmite on Anti-Ice Properties of Super-Hydrophobic Hierarchical Aluminum Surfaces. *Proceedings - Int. Workshop on Atmospheric Icing of Structures (IWAIS)*; Reykjavik, June 23−28, 2019.
(73) Calabrese, L.; Khaskhoussi, A.; Patane, S.; Proverbio, E. Assessment of Super-Hydrophobic Textured Coatings on AA6082 Aluminum Alloy. *Coatings* **2019**, *9*, 352.
(74) Kim, J.; Jun, S.; Lee, J.; Godinez, J.; You, S. M. Effect of Surface Roughness on Pool Boiling Heat Transfer of Water on a Superhydrophilic Aluminum Surface. *ASME. J. Heat Transfer.* **2017**, *139* (10), 101501 October.
(75) Saifaldeen, Z. S.; Khedir, K. R.; Cansizoglu, M. F.; et al. Superamphiphobic aluminum alloy surfaces with micro and nanoscale hierarchical roughness produced by a simple and environmentally friendly technique. *J. Mater. Sci.* **2014**, *49*, 1839−1853.
(76) Shur, V. Y.; Mingaliev, E. A.; Makaev, A. V.; Chezganov, D. S.; Kozheletova, I. Y.; Pryakhina, V. I. Creation of nanoparticles and surface nanostructures of alumina by hot water treatment. *IOP Conf. Ser.: Mater. Sci. Eng.* **2019**, *699*, 012051.
(77) Hu, Y.; Li, R.; Zhang, X.; Zhu, Y.; Nie, H.-Y. Aluminium films roughened by hot water treatment and derivatized by fluoroalkyl phosphonic acid: wettability studies. *Surface Engineering* **2020**, *36* (6), 589−600.
(78) Fiorilli, S.; Rivolo, P.; Descrovi, E.; Ricciardi, C.; Pasquardini, L.; Lunelli, L.; Vanzetti, L.; Pederzolli, C.; Onida, B.; Garrone, E. Vapor-phase self-assembled monolayers of aminosilane on plasma-activated silicon substrates. *J. Colloid Interface Sci.* **2008**, *321* (1), 235−241.
(79) Zhang, K.; Wu, J.; Chu, P.; Ge, Y.; Zhao, R.; Li, X. A novel CVD Method for Rapid Fabrication of Superhydrophobic Surface on Aluminum Alloy Coated Nanostructured Cerium-Oxide and Its Corrosion Resistance. *Int. J. Electrochem. Sci.* **2015**, *10* (8), 6257−6272.
(80) Wang, Z.; Gong, J.; Ma, J.; Xu, J. In Situ Growth of Hierarchical Boehmite on 2024 Aluminum Alloy Surface as Superhydrophobic. *RSC Adv.* **2014**, *4*, 14708−14714.
(81) Wang, L.; Wei, J.; Su, Z. Fabrication of Surfaces with Extremely High Contact Angle Hysteresis from Polyelectrolyte Multilayer. *Langmuir* **2011**, *27* (24), 15299−15304.
(82) Wang, R.; Nakasa, K.; Kubo, T.; Yamamoto, A.; Kaneko, J. Enhancement of Visible Light Absorbance and Hydrophobicity by Sputter-Coating of PTFE onto Fine Protrusions Formed by Sputter-Etching of Steels. *Materials Transactions* **2015**, *56* (1), 91−98.
(83) Huhtamäki, T.; Tian, X.; Korhonen, J. T.; Ras, R. H. A. Surface-Wetting Characterization Using Contact-Angle Measurements. *Nat. Protoc.* **2018**, *13* (7), 1521−1538.
(84) Stalder, A. F.; Melchior, T.; Müller, M.; Sage, D.; Blu, T.; Unser, M. Low-Bond Axisymmetric Drop Shape Analysis for Surface Tension and Contact Angle Measurements of Sessile Drops. *Colloids Surfaces A Physicochem. Eng. Asp.* **2010**, *364* (1−3), 72−81.
(85) Della Volpe, C.; Siboni, S.; Morra, M. Comments on Some Recent Papers on Interfacial Tension and Contact Angles. *Langmuir* **2002**, *18* (18), 1441−1444.
(86) Cassie, A. B. D.; Baxter, S. Wettability of Porous Surfaces. *Trans. Faraday Soc.* **1944**, *40*, 546−551.
(87) Marmur, A. Penetration and Displacement in Capillary Systems. In *Approaches to Wettability*; Schrader, M. E.; Loeb, G. I., Eds.; Springer: Boston, Massachusetts; 1992, DOI: 10.1007/978-1-4899-1176-6_12.

NOTE ADDED AFTER ASAP PUBLICATION

This paper was published ASAP on February 28, 2024, with errors in the expression for R_t in the Conclusions. The corrected version was reposted on February 29, 2024.

https://doi.org/10.1021/acsnano.3c05981
ACS Nano 2024, 18, 8626−8640